



OPEN

A new automatic geo-electric self-potential imaging technique for diverse sustainable development scenarios

Mahmoud Elhussein[✉] & Zein E. Diab[✉]

This study introduces a rapid and efficient inversion algorithm designed for the interpretation of self-potential responses originating from mineralized and ore sources and hydrothermal activity, specifically addressing spherical, vertical, and horizontal cylindrical structures. The algorithm leverages local wavenumber and correlation imaging techniques to enhance accuracy in modeling. The correlation factor (C_f value) is crucial in this approach, calculated as the correlation between the local wavenumber of the measured self-potential field and that of the computed field. The algorithm identifies the maximum correlation C_f value (C_f -max) as indicative of the optimal true model parameters. To validate the proposed algorithm, it was applied to three theoretical examples—one with contamination from regional background and another with multiple sources with and without different types of noises (random Gaussian and white Gaussian noises). Additionally, the approach was tested on three distinct real field cases related to mining, ore investigation and hydrothermal activity in India, Germany and USA. Through a comprehensive analysis of results from theoretical and real-world scenarios, including comparisons with different available data and literature information, the study concludes that the method is effective, applicable to multiple sources, accurate, and does not necessitate prior knowledge of the source shape. This algorithm presents a promising advancement in the field of self-potential interpretation for mineral exploration and geothermal exploration.

Keywords Self-potential, Imaging, Local wavenumber, Geothermal exploration, Mineral exploration

The self-potential (SP) or spontaneous polarization method stands out as an exceptionally passive approach within geophysics^{1–3}. It gauges the inherent potential difference (ΔV) beneath the surface, resulting from electrochemical, thermoelectric, and electrokinetic fields present within the Earth's interior^{4–7}. A myriad of geophysical challenges can be effectively addressed using the self-potential technique, encompassing tasks like delineating paleo-shear zones, mining, groundwater exploration, archaeology, geothermal investigation, and identifying underground voids^{8–11}.

Given the challenges arising from non-unique and ill-posed situations when interpreting self-potential anomalies linked to diverse mineralized sources, various inversion modeling methods have been devised to tackle these issues^{5,12,13}. These inversion techniques primarily entail approximating the various geoelectric sources through uncomplicated geometric configurations to deduce structural parameters^{6,14–17}. These methodologies encompass a range of strategies such as the linear and non-linear inversion approach^{18–20}, utilization of nomograms and the graphical approach^{21–24}, neural networks²⁵, and gradient approach^{11,26}. Many of these methods necessitate prior knowledge about the model's parameters and a suitable parameter search range to find optimal solutions. Pateela²⁷ introduced SP tomography^{28,29}, a technique that entails scanning a segment within an SP survey profile utilizing a basic charge unit of uniform strength. This charge is administered across a systematic grid of spatial coordinates, and the probability function for charge occurrence is computed at each individual point. The resulting set of grid values enables the creation of contour lines, aiding in identifying areas with the highest probability of concentrated polarized, primary, and secondary electric charges. However, utilizing this approach to calculate the depth of a source necessitates access to the structural index of the causative source, a task that proves challenging in the case of an unfamiliar region³⁰.

Department of Geophysics, Faculty of Science, Cairo University, P.O. 12613, Giza, Egypt. ✉email: melhussein@cu.edu.eg; zdiab@cu.edu.eg

The more recent advancements include techniques like genetic algorithms^{31,32}, black hole technique³³, particle swarm optimization (PSO)^{6,34}, grey wolf optimization³⁵, simulated and very fast simulated annealing^{31,36}. These methods provide a primary benefit by efficiently exploring extensive solution spaces without requiring prior familiarity with the underlying structure of the problem. However, some of these methods face challenges when dealing with multi-structure optimization. Additionally, others may face issues in achieving enhanced search output, necessitating tuning of parameters. An enhanced control strategy is required to adeptly transition between exploration and exploitation³⁷. While these techniques do not ensure the discovery of the optimal outcome, their objective is to identify optimal solutions within a reasonable timeframe³⁸.

This study has introduced an effective imaging algorithm that has been devised to comprehensively interpret self-potential data stemming from diverse subterranean structures like horizontal cylinders, spheres, and vertical cylinders. This method hinges on the computation of the correlation factor (C_f) between the local wavenumber of the observed self-potential anomaly and that of the calculated anomaly. The model associated with the highest C_f value (C_f -max) is deemed the most accurate model. This strategy has potential applications in diverse fields such as mineral and ore exploration, as it aids in determining various structural parameters including amplitude factor (K), depth (z_o), body origin (x_o), shape factor (q), and polarization angle (θ) all without requiring any prior knowledge of the source shape. Furthermore, this technique can also be extended to estimating parameters from multiple sources. In order to validate the effectiveness and practicality of this proposed approach, the method was employed to analyze self-potential data from three theoretical scenarios with and without different types of noises, as well as three field examples from India, Germany and USA.

Methodology

The self-potential signature (P) at an observation point (x, z) along the profile depicted in Fig. 1, can be expressed using the formula of Yüngül³⁹.

$$P(K, x_j, x_o, z_o, \theta, q) = K \frac{(x_l - x_o)\cos\theta + z_o\sin\theta}{[(x_l - x_o)^2 + z_o^2]^q}, j = 1, 2, 3, \dots, n \quad (1)$$

where n represents the count of data points, q is the shape factor, a dimensionless quantity, varies according to the structure's shape (it takes a value of 1.5 for a structure resembling a sphere, 1 for a horizontal cylindrical structure, and 0.5 for a semi-infinite vertical cylinder). The depth of the structure is denoted as ' z_o ' in meters. The amplitude factor (K), with unit mVm^{2q-1} , the parameter ' x_o ' indicates the position of the source body in meters, and ' θ ' corresponds to the polarization angle in degrees.

The measured local wavenumber can be formulated by^{30,40}:

$$LW_{mea} = \frac{\partial \varnothing}{\partial x}, \quad (2)$$

where

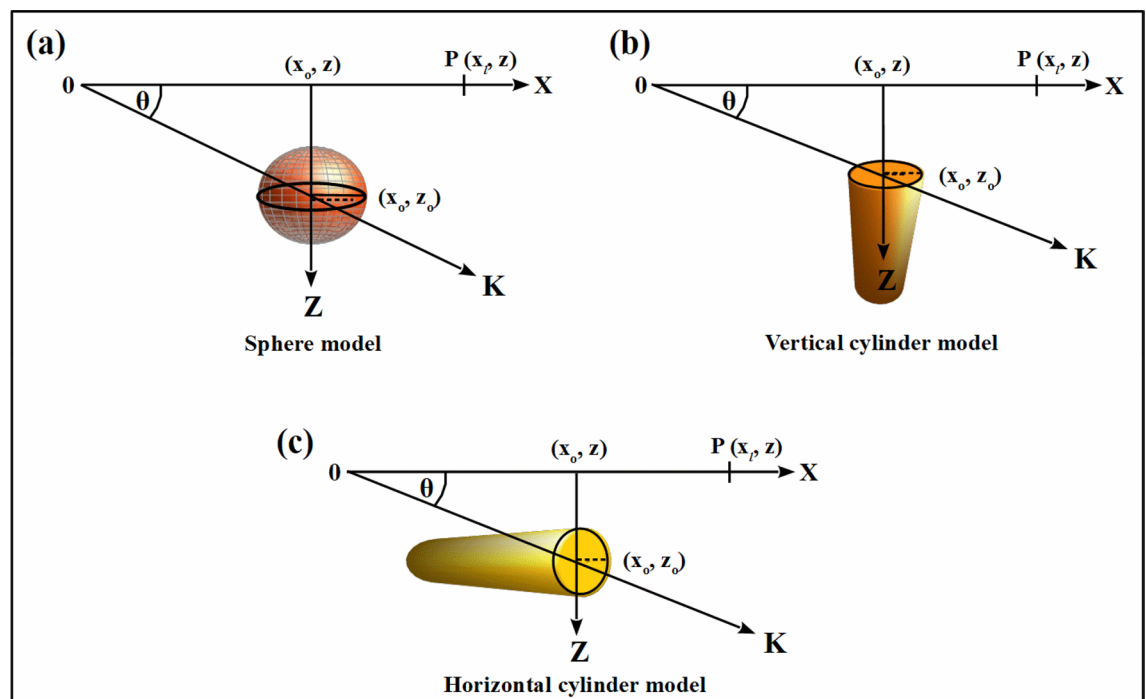


Figure 1. Different geometric structures for various basic shapes include (a) sphere, (b) vertical cylinder, (c) horizontal cylinder.

$$\varnothing = \tan^{-1} \left[\frac{\left(\frac{\partial P}{\partial z} \right)}{\left(\frac{\partial P}{\partial x} \right)} \right], \quad (3)$$

By substitution (Eq. 3 in Eq. 2), LW_{mea} can be given by:

$$LW_{mea} = \frac{\partial}{\partial x} \tan^{-1} \left[\frac{\left(\frac{\partial P}{\partial z} \right)}{\left(\frac{\partial P}{\partial x} \right)} \right] = \frac{1}{AS^2} \left[\left(\frac{\partial^2 P}{\partial x \partial z} \cdot \frac{\partial P}{\partial x} \right) - \left(\frac{\partial^2 P}{\partial x^2} \cdot \frac{\partial P}{\partial z} \right) \right], \quad (4)$$

where AS is the analytical signal amplitude as follow⁴¹:

$$AS = \sqrt{\left(\frac{\partial P}{\partial x} \right)^2 + \left(\frac{\partial P}{\partial z} \right)^2}, \quad (5)$$

By applying the horizontal and vertical derivatives $\left(\frac{\partial P}{\partial x} \right)$ and $\left(\frac{\partial P}{\partial z} \right)$ respectively to Eq. (1) and substituting in Eq. (4), the computed local wavenumber (LW_{com}) is given by:

$$LW_{com} = \frac{-2qz_o \left[((x_l - x_o)^2 + z_o^2) \left(\frac{q}{q-1} - \cos 2\theta \right) + 2z_o(x_l - x_o) \sin 2\theta \right]}{((x_l - x_o)^2 + z_o^2) \left[\frac{1}{q-1} + 2q \left(((x_l - x_o)^2 - z_o^2) \cos 2\theta + 2z_o(x_l - x_o) \sin 2\theta + 1 \right) \right]}, \quad (6)$$

Using LW_{mea} and LW_{com} , the correlation parameter can be represented by^{30,40}:

$$C_F = \frac{\sum_{j=1}^n |LW_{mea}|_j |LW_{com}|_j}{\sqrt{\sum_{j=1}^n |LW_{mea}|_j^2 \sum_{j=1}^n |LW_{com}|_j^2}}. \quad (7)$$

Using Eq. (7), the calculation of the correlation parameter (C_F) between LW_{mea} and LW_{com} is performed, and the highest value of C_F corresponds to actual body characteristics^{30,40}. The process flow of the proposed algorithm is illustrated in Fig. 2. After identifying the most suitable parameters from the search space based on the highest C_F value (C_F -max), it becomes possible to create a two-dimensional representation of C_F for the preferred source (specifically, the shape factor q) in relation to subsurface depth (m). The solid black dot present in the imaging section symbolizes the accurate position for both depth and location.

Synthetic models

This segment demonstrates the application of the suggested method to three distinct synthetic models, both with and without noise, in order to assess the effectiveness and suitability of the proposed approach in the interpretation of self-potential anomalies.

Example 1

The self-potential profile resulting from a horizontal cylinder was computed with specific parameters: $K = 3500$ mV m, $z_o = 10$ m, $x_o = 0$ m, $q = 1$, and $\theta = -55^\circ$, over a profile length of 100 m (depicted in Fig. 3a). The interpretation process began by calculating both horizontal and vertical gradients of the observed anomaly (as shown in Fig. 3b). Subsequently, the value of LW_{mea} was determined using Eq. (4) (illustrated in Fig. 3c). Moving forward, the calculation of C_f was carried out using Eq. (7) (as demonstrated in Fig. 3d), considering various q values as presented in Table 1. Notably, in Table 2, the highest value of C_f (C_F -max = 1) (black circle in Fig. 3d) is located at $K = 3500$ mV m, $z_o = 10$ m, $x_o = 0$ m, $q = 1$, and $\theta = -55^\circ$, which aligns with the information in Fig. 3d. This outcome signifies the exceptional efficiency of the proposed method. Utilizing the suggested approach facilitated the estimation of inverted parameters as detailed in Table 2, leading to a complete absence of errors for the diverse parameters.

To assess the robustness and effectiveness of the suggested method when applied to data with noise, the method was applied to the previous model after adding 15% random Gaussian noise (RGN) and 15% white Gaussian noise (WGN). Firstly, 15% RGN (Fig. 4a), the noisy data's vertical and horizontal gradients were computed (Fig. 4b). Subsequently, utilizing Eq. (4), LW_{mea} was determined (Fig. 4c). To derive C_f , Eq. (7) was employed (Fig. 4d). Within Fig. 4d, the highest C_f value of 0.8075 (depicted by the black circle in Fig. 4d) is observed at $K = 3948$ mV m, $z_o = 11.5$ m, $x_o = -1$ m, $q = 1$, and $\theta = -54^\circ$, as indicated in Table 3. The computed error of the estimated parameters, K , z_o , q , θ are: 12.8%, 15%, 0% and 1.82% respectively.

Secondly, 15% WGN (Fig. 5a), the noisy data's vertical and horizontal gradients were computed (Fig. 5b). Subsequently, applying Eq. (4), LW_{mea} was determined (Fig. 5c). To derive C_f , Eq. (7) was employed (Fig. 5d). Within Fig. 5d, the highest C_f value of 0.6784 (depicted by the black circle in Fig. 5d) is observed at $K = 4015$ mV m, $z_o = 12$ m, $x_o = -1$ m, $q = 1$, and $\theta = -54.5^\circ$, as indicated in Table 3. The computed error of the estimated parameters, K , z_o , q , θ are: 14.7%, 20%, 0% and 0.91% respectively. The results obtained above shows that the effect of the WGN is greater than RGN on the proposed method but the estimated parameters in case of the different two types of noise demonstrating that the proposed method can effectively be employed to handle noisy data with exceptional performance.

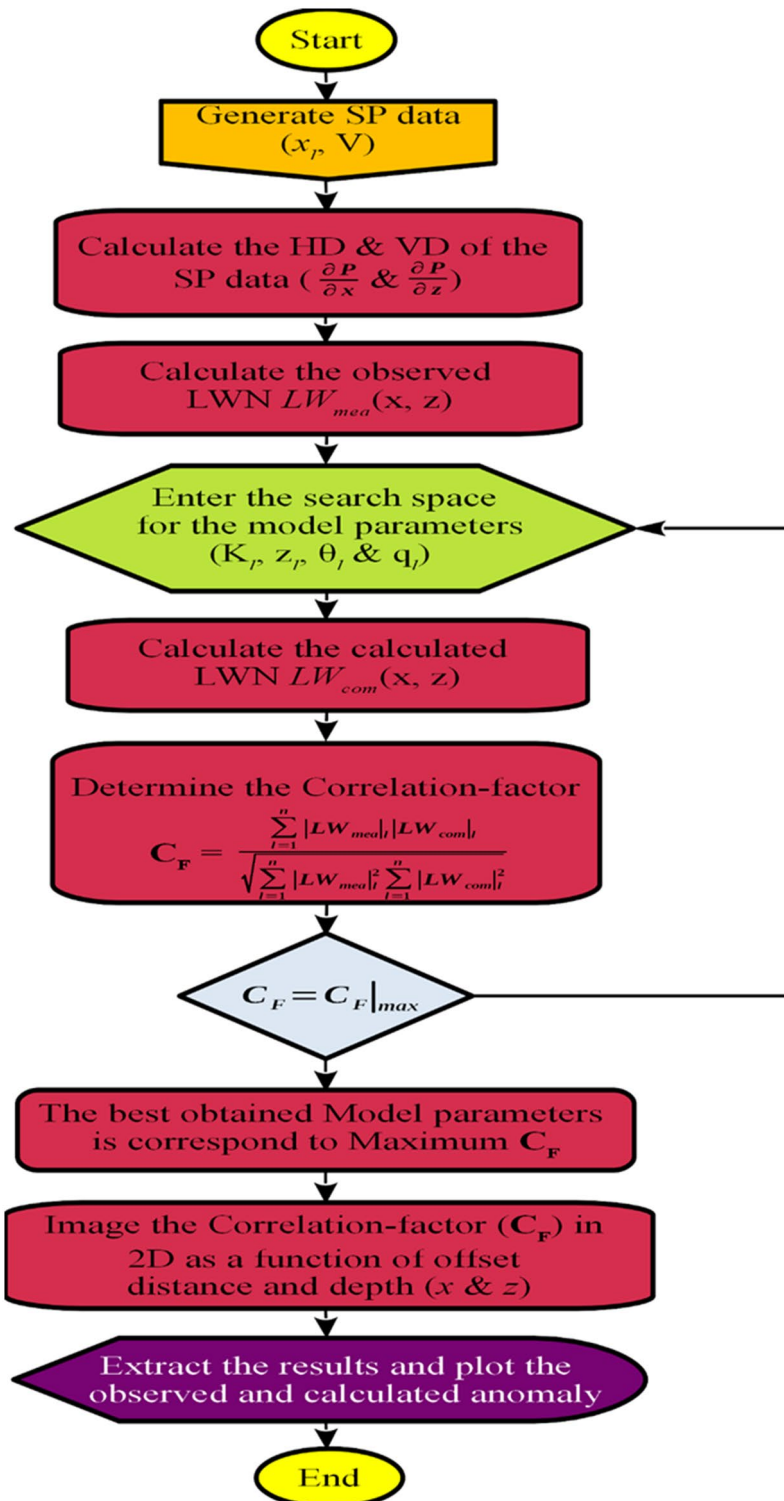


Figure 2. Flowchart depicting the procedural sequence of the algorithm under consideration.

Example 2

In order to evaluate the suitability and effectiveness of the employed approach when dealing with multisource examples, the technique was implemented on a 100 m composite profile that was constructed of sphere body (applying these parameters: $K = 30,500 \text{ mV m}^2$, $z_o = 5 \text{ m}$, $x_o = -30 \text{ m}$, $q = 1.5$, and $\theta = -25^\circ$) and horizontal-cylinder (HC) body (applying these specific parameters: $K = 2500 \text{ mV m}$, $z_o = 3 \text{ m}$, $x_o = 30 \text{ m}$, $q = 1$, and $\theta = -35^\circ$) (Fig. 6a). The process of interpretation began with the computation of both the vertical and horizontal gradients of the composite profile (depicted in Fig. 6b). The value LW_{mea} was determined applying Eq. (4) (illustrated

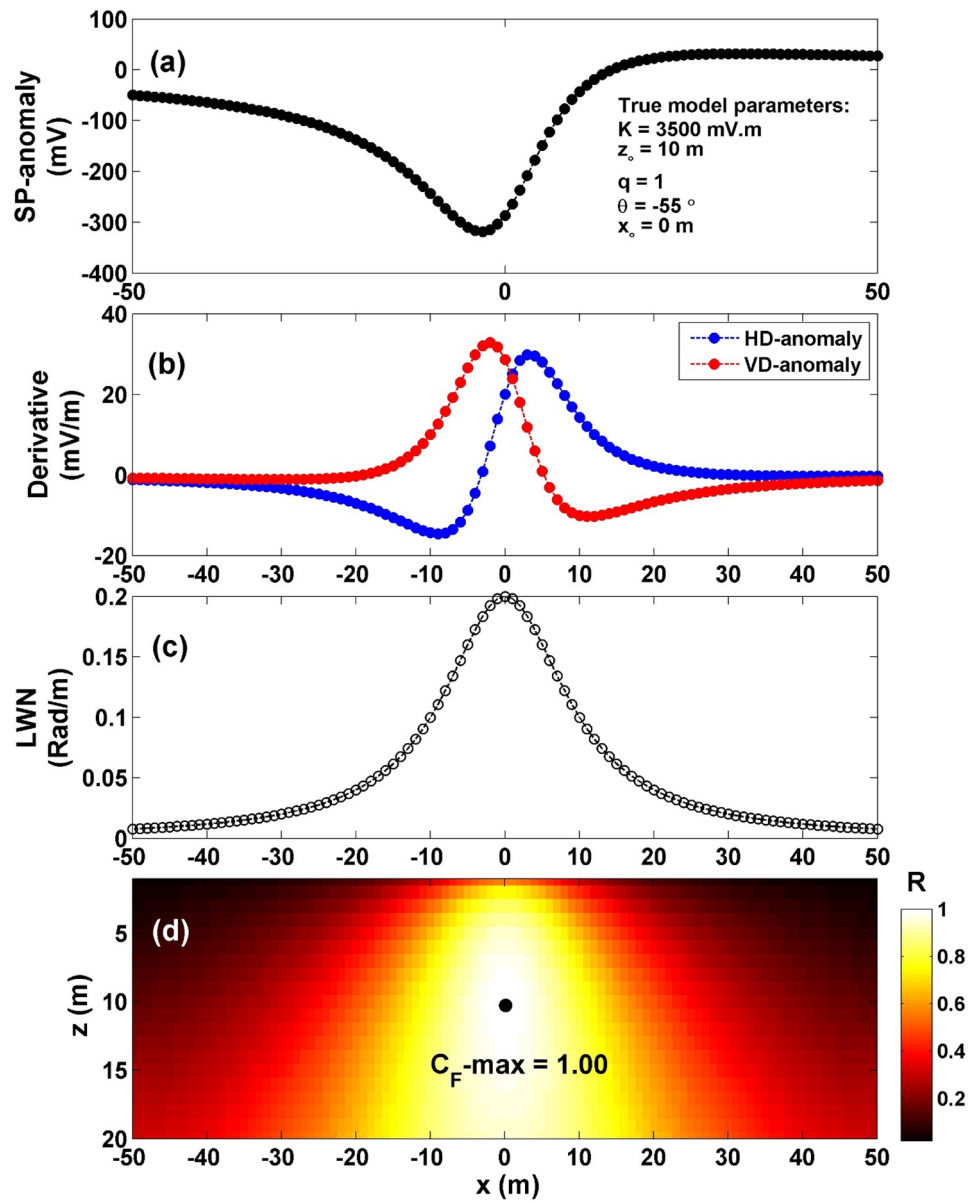


Figure 3. (a) Profile of the self-potential anomaly induced by a horizontal cylinder, (b) computed horizontal and vertical derivatives for the profile depicted in (a), (c) local wavenumber of the data depicted in (b), (d) visualizing the correlation factor (C_F) and determining the C_F -max through the newly established method.

Geometric shape factor	Maximum correlation factor
(q)	(C_F -max)
0.5	0.9242
1	1.0000
1.5	0.9995

Table 1. The correlation factor (C_F) calculated at the different shape factors for the first theoretical example (self-potential anomaly induced by a horizontal cylinder). The optimum values are in [bold].

Model parameters	True	Recovered
K (mV m)	3500	3500
z_0 (m)	10	10
x_0 (m)	0	0
q	1.0	1.0
θ (°)	-55	-55
C_F -max		1.0000

Table 2. The authentic and retrieved model parameters pertaining to the first theoretical example (self-potential anomaly generated by a horizontally cylinder).

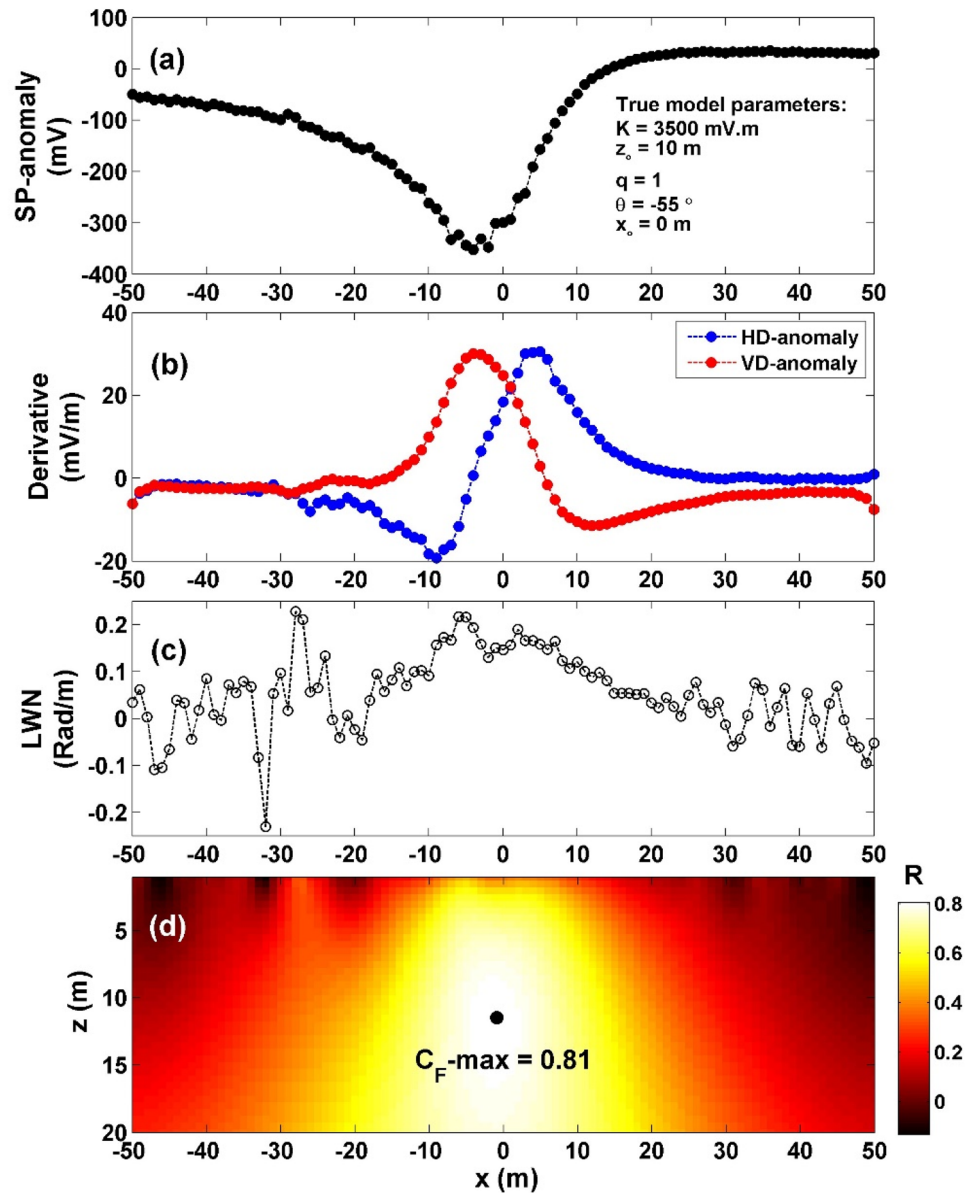


Figure 4. (a) Profile of the self-potential anomaly depicted in Fig. 3a after contaminating with 15% RGN, (b) computed horizontal and vertical derivatives for the profile depicted in (a), (c) local wavenumber of the data depicted in (b), (d) visualizing the correlation factor (C_F) and determining the C_F -max through the newly established method.

Model parameters	True	Recovered	
		15% RGN	15% WGN
K (mV m)	3500	3948	4015
z_o (m)	10	11.5	12
x_o (m)	0	-1	-1
q	1.0	1.0	1.0
θ (°)	-55	-54	-54.5
C_F -max		0.8075	0.6784

Table 3. The authentic and retrieved model parameters pertaining to the first theoretical example (self-potential anomaly generated by a horizontally cylinder) contaminated with 15% RGN and 15% WGN.

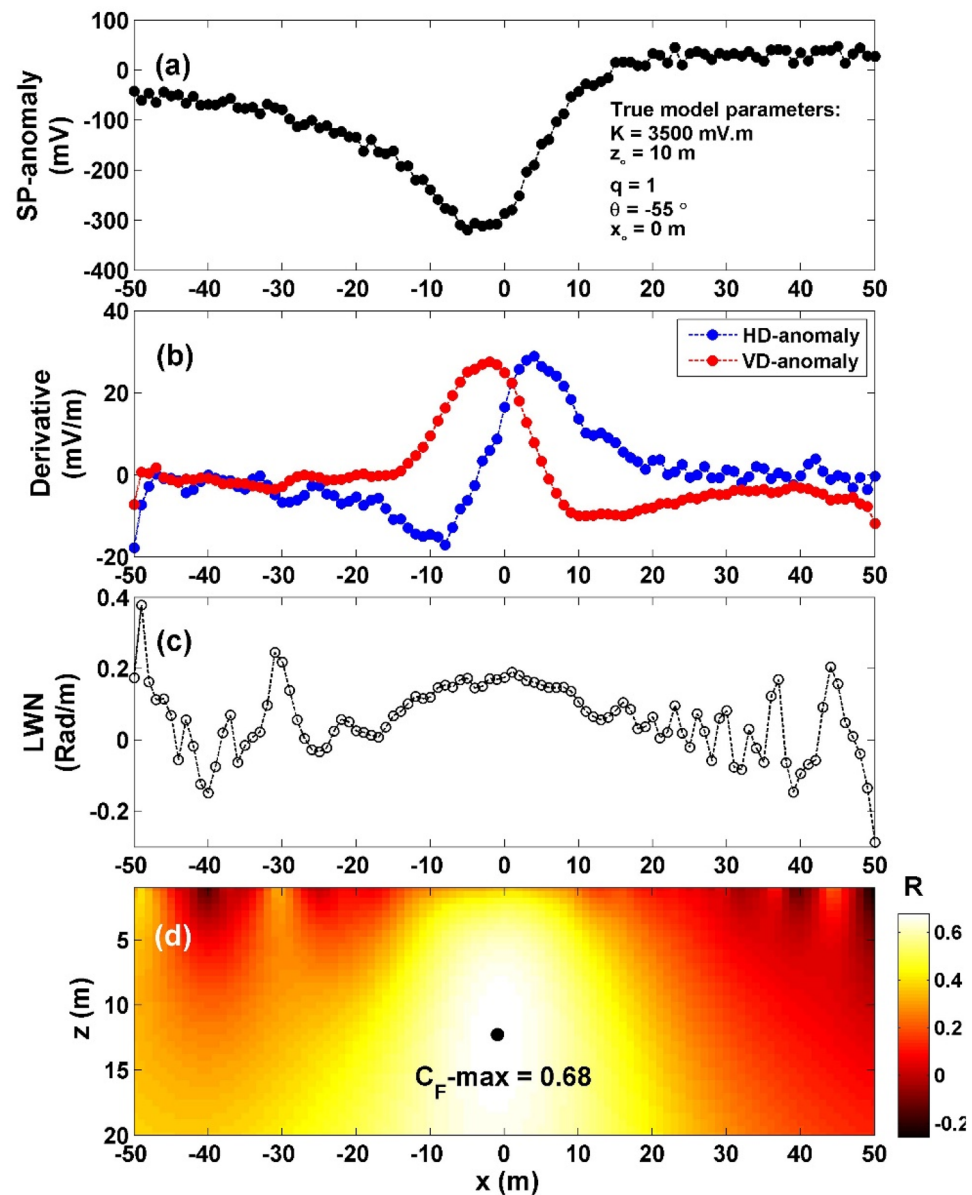


Figure 5. (a) Profile of the self-potential anomaly depicted in Fig. 3a after contaminating with 15% WGN, (b) computed horizontal and vertical derivatives for the profile depicted in (a), (c) local wavenumber of the data depicted in (b), (d) visualizing the correlation factor (C_F) and determining the C_F -max through the newly established method.

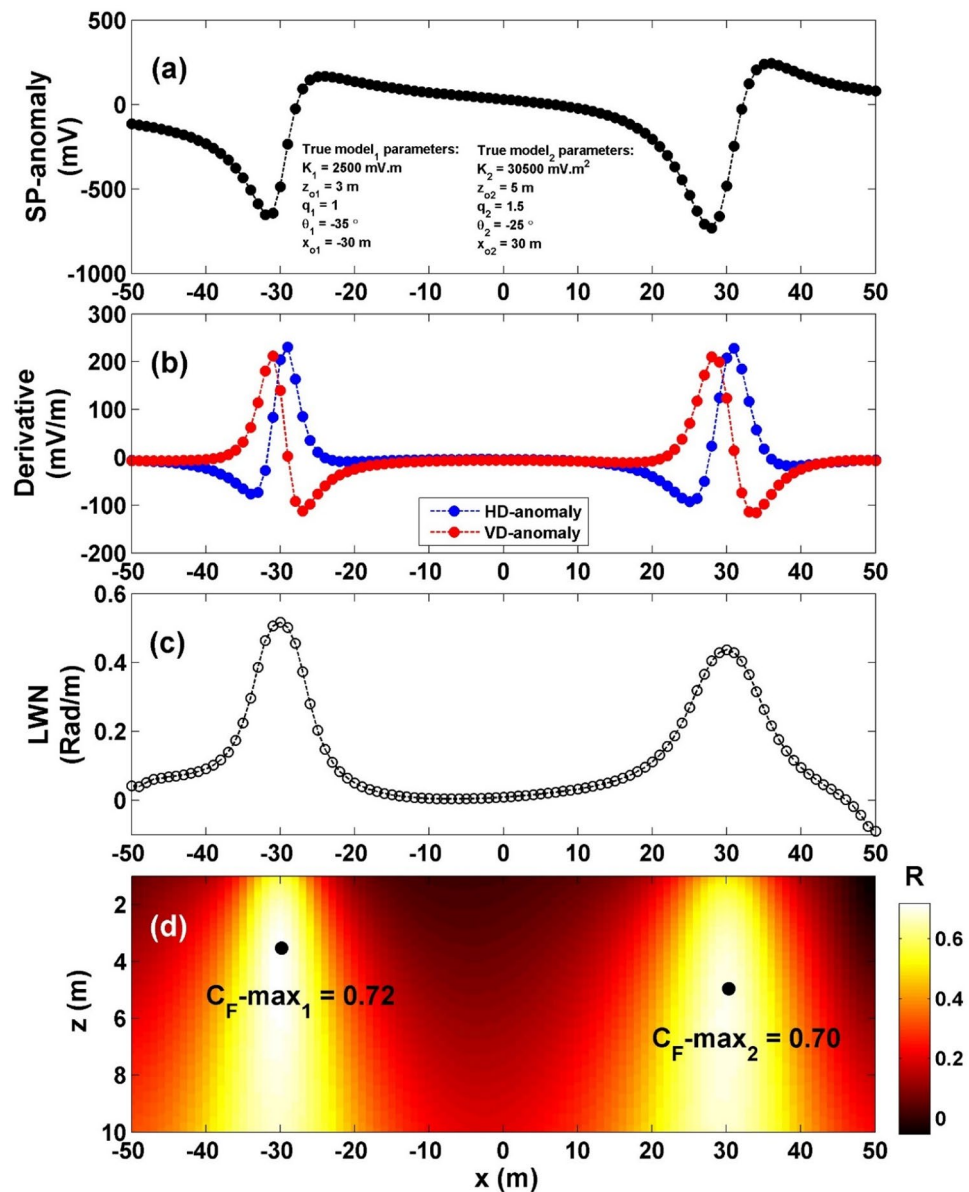


Figure 6. (a) Profile of the self-potential anomaly induced by multisource models of sphere and horizontal cylinder, (b) computed horizontal and vertical derivatives for the profile depicted in (a), (c) local wavenumber of the data depicted in (b), (d) visualizing the correlation factor (C_f) and determining the $C_F\text{-max}$ through the newly established method.

in Fig. 6c), while the value of C_f was calculated using Eq. (7) (as shown in Fig. 6d). It is demonstrated that the highest C_f value ($C_F\text{-max}_1$) for the sphere body is 0.74 (indicated by the initial black circle in Fig. 6d), situated at $K = 27,718 \text{ mV m}^2$, $z_o = 4.9 \text{ m}$, $x_o = -30 \text{ m}$, $q = 1.5$, and $\theta = -24.71^\circ$ (Table 4). Similarly, the maximum C_f value ($C_F\text{-max}_2$) for the HC body is 0.70 (depicted by the second black circle in Fig. 6d), located at $K = 2636 \text{ mV m}$, $z_o = 3.4 \text{ m}$, $x_o = 30 \text{ m}$, $q = 1$, and $\theta = -38.79^\circ$, as summarized in Table 4. The computed error of the estimated parameters, K , z_o , x_o , q , and θ are: 9.12%, 2%, 0%, 0% and 1.16% respectively for the sphere body, while for the HC source, the computed error of the estimated parameters, K , z_o , x_o , q , and θ are: 5.44%, 13.33%, 0%, 0% and 10.83%, respectively.

To evaluate how well the proposed method performs in the presence of noise and its overall effectiveness, the method was applied to the previous model after adding 10% RGN and 10% WGN. The first case, 10% RGN (Fig. 7a), the noisy composite data's vertical and horizontal gradients were computed (Fig. 7b). The value LW_{mea} was determined (illustrated in Fig. 7c), while the value of C_f was calculated (as shown in Fig. 7d). It is demonstrated that the highest C_f value ($C_F\text{-max}_1$) for the sphere body is 0.55 (indicated by the initial black circle in Fig. 7d), situated at $K = 23,287 \text{ mV m}^2$, $z_o = 4.6 \text{ m}$, $x_o = -30 \text{ m}$, $q = 1.5$, and $\theta = -26.01^\circ$ (Table 5). Similarly, the maximum C_f value ($C_F\text{-max}_2$) for the HC body is 0.56 (depicted by the second black circle in Fig. 7d), located at $K = 2293 \text{ mV m}$, $z_o = 3.2 \text{ m}$, $x_o = 30 \text{ m}$, $q = 1$, and $\theta = -42.67^\circ$, as summarized in Table 5. The computed error of

Model parameters	True		Recovered	
	HC model	Sphere model	HC model	Sphere model
K (mV m ^{2q-1})	2500 mV m	30,500 mV m ²	2636 mV m	27,718 mV m ²
z _o (m)	3	5	3.4	4.9
x _o (m)	30	- 30	30	- 30
q	1.0	1.5	1.0	1.5
θ (°)	- 35	- 25	- 38.79	- 24.71
C _F -max			0.72	0.70

Table 4. The authentic and retrieved model parameters pertaining to the second theoretical example (induced by multisource models of sphere and horizontal cylinder).

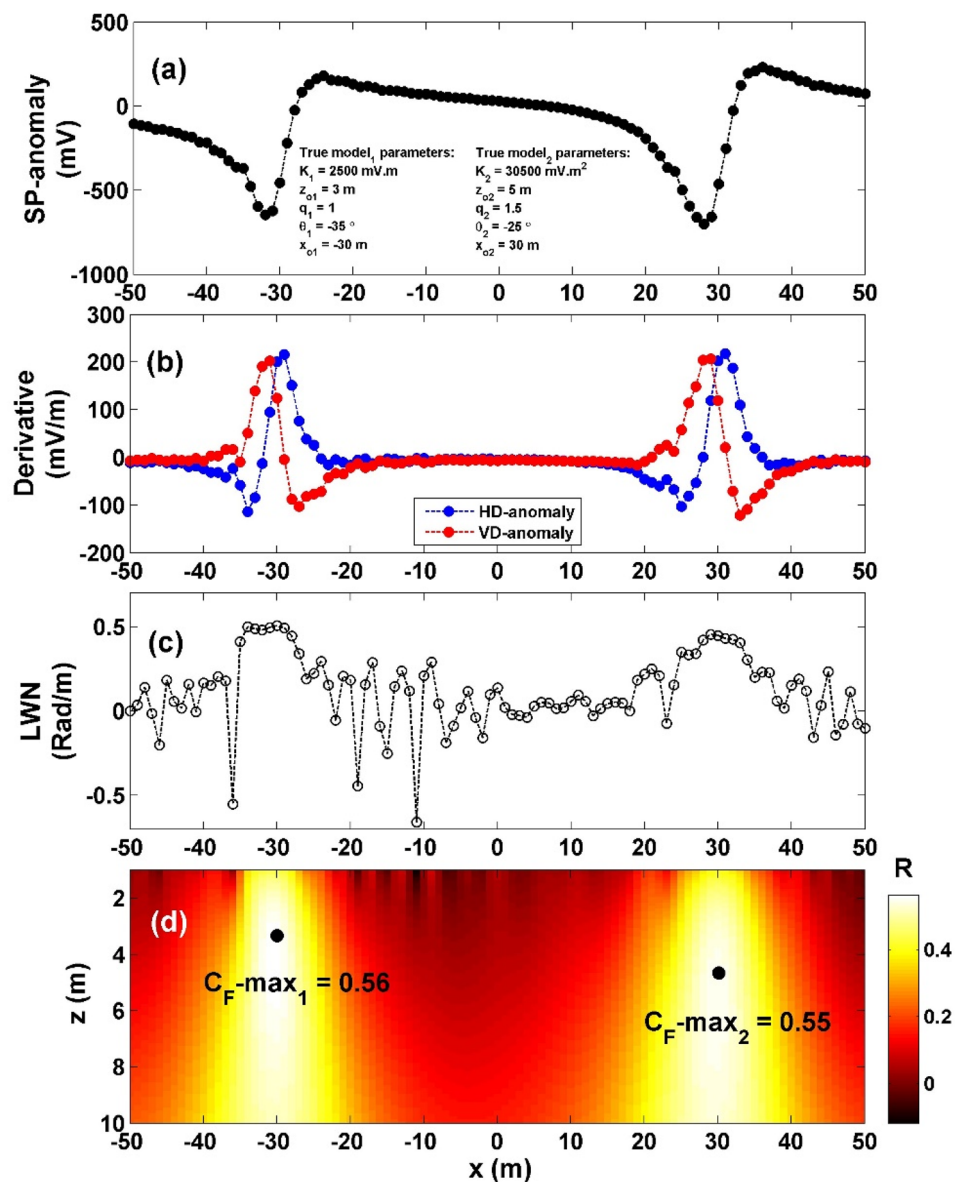


Figure 7. (a) Profile of the self-potential anomaly depicted in Fig. 6a after contaminating with 10% RGN, (b) computed horizontal and vertical derivatives for the profile depicted in (a), (c) local wavenumber of the data depicted in (b), (d) visualizing the correlation factor (C_F) and determining the C_F-max through the newly established method.

Model parameters	True		Recovered [RGN 10%]		Recovered [WGN 10%]	
	HC model	Sphere model	HC model	Sphere model	HC model	Sphere model
K (mV m ^{2q-1})	2500 mV m	30,500 mV m ²	2293 mV m	23,287 mV m ²	2833 mV m	36,322 mV m ²
z_o (m)	3	5	3.2	4.6	4.3	5.9
x_o (m)	30	- 30	30	- 30	30	- 30
Q	1.0	1.5	1.0	1.5	1.0	1.5
θ (°)	- 35	- 25	- 42.67	- 26.01	- 47.50	- 27.55
C_F -max			0.56	0.55	0.48	0.50

Table 5. The authentic and retrieved model parameters pertaining to the second theoretical example (induced by multisource models of sphere and horizontal cylinder) contaminated with 10% RGN and 10% WGN.

the estimated parameters, K , z_o , x_o , q , and θ are: 23.65%, 8%, 0%, 0% and 4.04% respectively for the sphere body, while for the HC source, the computed error of the estimated parameters, K , z_o , x_o , q , and θ are: 8.28%, 6.67%, 0%, 0% and 21.91%, respectively.

The second case, 10% WGN (Fig. 8a), the noisy composite data's vertical and horizontal gradients were computed (Fig. 8b), The value LW_{mea} was determined (illustrated in Fig. 8c), while the value of C_f was calculated (as shown in Fig. 8d). It is demonstrated that the highest C_f value (C_F -max₁) for the sphere body is 0.50 (indicated by the initial black circle in Fig. 8d), situated at $K=36,322$ mV m², $z_o=5.9$ m, $x_o=-30$ m, $q=1.5$, and $\theta=-27.55^\circ$ (Table 5). Similarly, the maximum C_f value (C_F -max₂) for the HC body is 0.48 (depicted by the second black circle in Fig. 8d), located at $K=2833$ mV m, $z_o=4.3$ m, $x_o=30$ m, $q=1$, and $\theta=-47.50^\circ$, as summarized in Table 5. The computed error of the estimated parameters, K , z_o , x_o , q , and θ are: 19.09%, 18%, 0%, 0% and 10.2% respectively for the sphere body, while for the HC source, the computed error of the estimated parameters, K , z_o , x_o , q , and θ are: 13.32%, 43.33%, 0%, 0% and 35.71%, respectively.

Hence, it can be inferred that the suggested approach is well-suited for scenarios involving multiple sources.

Example 3

To assess the effectiveness of our approach when dealing with a regional context, we introduced a self-potential anomaly profile originating from a vertical cylinder (characterized by: $K=250$ mV, $z_o=4$ m, $x_o=-25$ m, $q=0.5$, and $\theta=-75^\circ$ and profile length 100 m) into a deep-seated first order regional anomaly (Fig. 9a). The interpretation process commenced by computing both the horizontal and vertical gradients of the observed anomaly, as depicted in Fig. 9b. Subsequently, Eq. (4), was employed to ascertain the value of LW_{mea} (Fig. 9c). Moving forward, Eq. (7) was utilized, to calculate C_f (Fig. 9d). It's worth noting that in Table 6, the highest value of C_f (C_F -max=0.93), denoted by a black circle in Fig. 9d, corresponds to $K=296.58$ mV, $z_o=4.5$ m, $x_o=-25$ m, $q=0.5$, and $\theta=-75^\circ$. The computed error of the estimated parameters, K , z_o , x_o , q , and θ are: 18.63%, 12.5%, 0%, 0% and 0%, respectively.

To evaluate the robustness and efficacy of the proposed method when applied to noisy data, we introduced two types of noise, specifically, 15% RGN and 15% WGN, to the previous model.

In the case of 15% RGN (depicted in Fig. 10a), we initially computed the vertical and horizontal gradients of the noisy data (Fig. 10b). Subsequently, using Eq. (4), we calculated LW_{mea} (Fig. 10c). The determination of C_f was carried out using Eq. (7) (Fig. 10d). Within Fig. 10d, the highest C_f value (C_F -max=0.55) indicated by the black circle in Fig. 10d) was observed at specific parameter values: $K=306.56$ mV, $z_o=4.8$ m, $x_o=-25$ m, $q=0.5$, and $\theta=-71.65^\circ$, as presented in Table 7. The computed errors for the estimated parameters K , z_o , x_o , q , and θ were found to be 22.62%, 20%, 0%, 0%, and 4.47%, respectively.

Moving on to the scenario with 15% WGN (illustrated in Fig. 11a), we again computed the vertical and horizontal gradients of the noisy data (Fig. 11b). Subsequently, employing Eq. (4), we determined LW_{mea} (Fig. 11c). To derive C_f , Eq. (7) was utilized (Fig. 11d). Within Fig. 11d, the highest C_f value (C_F -max=0.588), depicted by the black circle in Fig. 11d was observed at specific parameter values: $K=293.31$ mV, $z_o=5.1$ m, $x_o=-25$ m, $q=0.5$, and $\theta=-71.13^\circ$, as indicated in Table 7. The computed errors for the estimated parameters K , z_o , x_o , q , and θ were found to be 17.32%, 27.5%, 0%, 0%, and 5.16%, respectively.

Field models

In order to evaluate the effectiveness of the suggested method, it was employed in three distinct real-life field data, including one from India, one from Germany and the third from USA.

India field example (Neem-Ka-Thana Copper Belt)

The Neem-Ka-Thana Copper Belt in India is distinguished by the prevalence of copper mineralization in the region^{4,42}. Notably, the copper deposits are primarily located along fault lines and shear planes, indicating a geological association with these structural features. The concentration of copper in the mines within the Neem-Ka-Thana Copper Belt shows variability, ranging from 0.6 to 1.2%^{4,43}. This diversity in copper content underscores the geological complexity of the region, suggesting that mineralization processes have been influenced by a combination of tectonic forces and geological phenomena. Therefore, the Neem-Ka-Thana Copper Belt stands out as a significant geological site where the interplay of geological structures and mineralization processes contributes to the formation of valuable copper deposits.

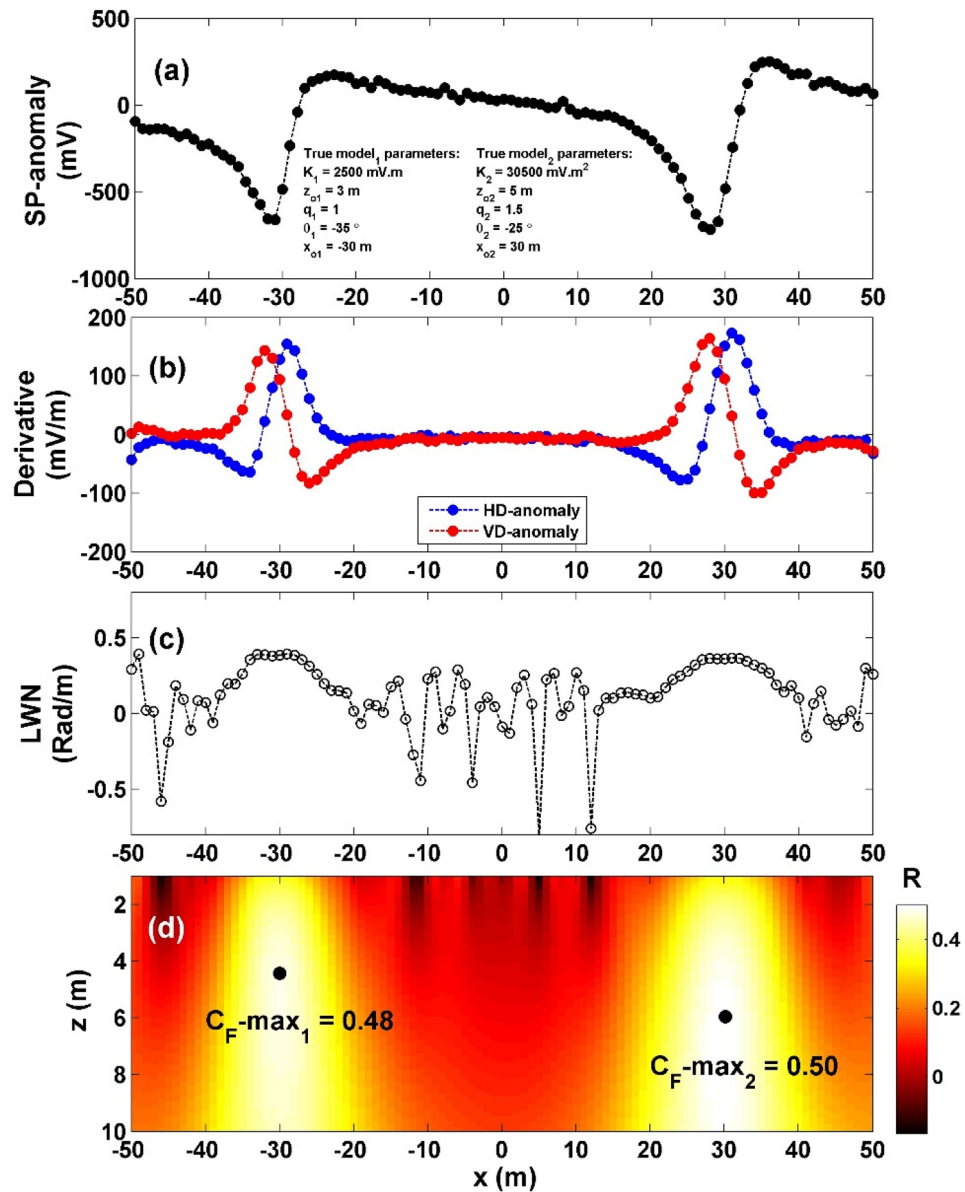


Figure 8. (a) Profile of the self-potential anomaly depicted in Fig. 6a after contaminating with 10% WGN, (b) computed horizontal and vertical derivatives for the profile depicted in (a), (c) local wavenumber of the data depicted in (b), (d) visualizing the correlation factor (C_F) and determining the C_F -max through the newly established method.

A profile of self-potential was acquired over the Neem-Ka-Thana Copper Belt in India^{43,43} (Fig. 12a). The profile length was 285 m long. The interpretation procedure initiated with the computation of both the horizontal and vertical gradients of the observed anomaly, illustrated in Fig. 12b. Following this, Eq. (4) was applied to determine the value of LW_{mea} , as shown in Fig. 12c. Progressing further, Eq. (7) was employed to compute C_F , depicted in Fig. 12d, considering various q values as presented in Table 8. It is noteworthy that Table 8 presents the maximum value of C_F ($C_F\text{-max} = 0.96$), represented by a black circle in Fig. 12d, corresponding to $K = -47.92 \text{ mV}$, $z_o = 18 \text{ m}$, $x_o = 177.5 \text{ m}$, $q = 0.4$, and $\theta = 88^\circ$ (Table 9). The comparison between the results obtained by our suggested method and those obtained by Balkaya⁴⁴ is depicted in Fig. 12a. Table 9 displays a comparison of the inverted parameters between the proposed method and those of different methods found in the literature.

Germany field example (Lias-epsilon black shales)

The Lias-epsilon black shales in Germany are situated atop a coal maturity high on the Bramsche Massif in Northwest Germany, as described by⁴⁵. The thermal evolution of this region is attributed to the inversion of the Lower Saxony Basin, occurring during the Early Late Cretaceous period, likely in conjunction with mafic intrusions from the Bramsche, Vlotho, and Uchte Massifs at depths of approximately 5–10 km^{46–48}.

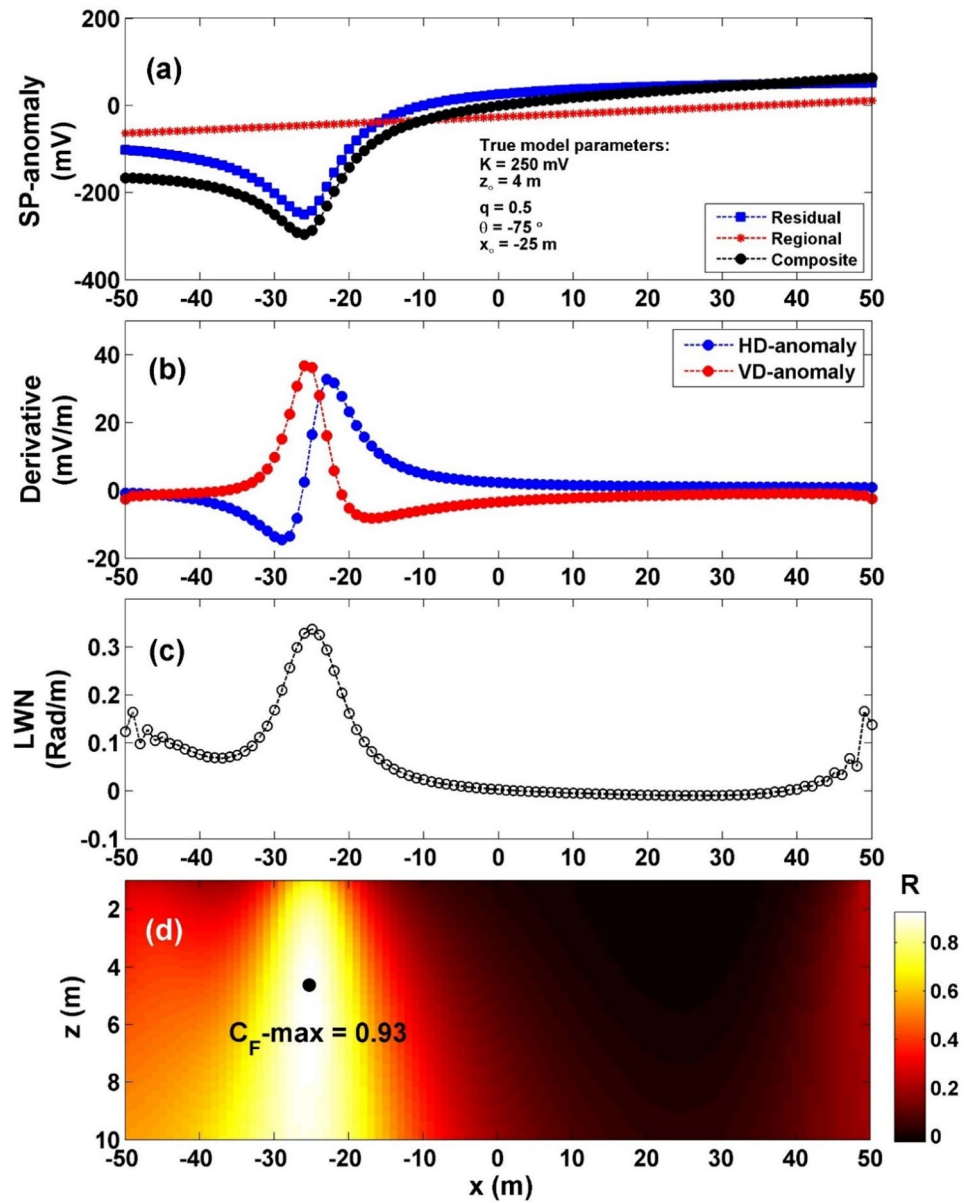


Figure 9. (a) Profile of the self-potential composite anomaly induced by vertical cylinder and first order regional source, (b) computed horizontal and vertical derivatives for the profile depicted in (a), (c) local wavenumber of the data depicted in (b), (d) visualizing the correlation factor (C_f) and determining the $C_{F\text{-max}}$ through the newly established method.

Model parameters	True	Recovered
K (mV)	250	296.58
z_o (m)	4	4.5
x_o (m)	-25	-25
q	0.5	0.5
θ ($^\circ$)	-75	-75
$C_{F\text{-max}}$		0.9266

Table 6. The authentic and retrieved model parameters pertaining to the second theoretical example (self-potential composite anomaly induced by vertical cylinder and first order regional source).

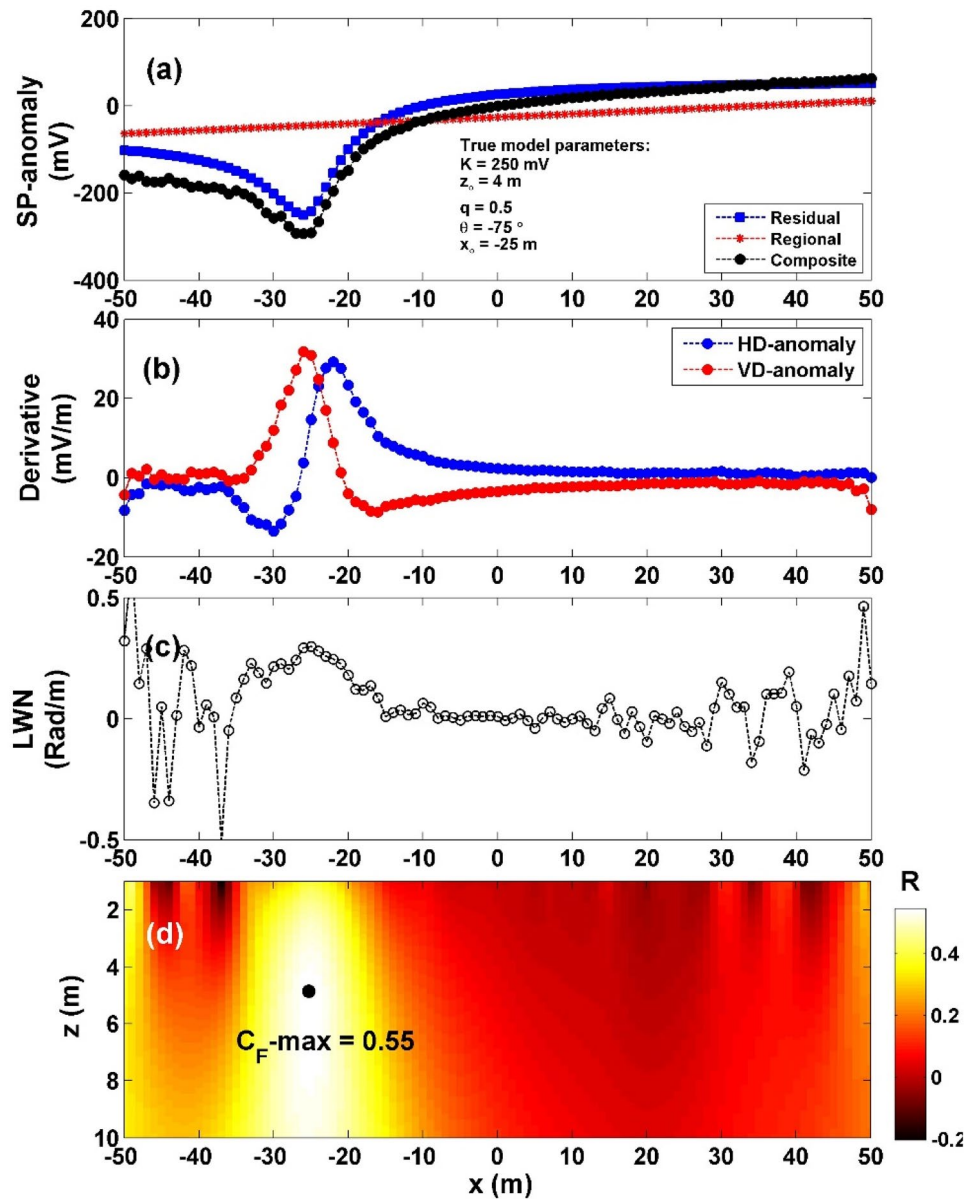


Figure 10. (a) Profile of the self-potential anomaly depicted in Fig. 9a after contaminating with 15% RGN, (b) computed horizontal and vertical derivatives for the profile depicted in (a), (c) local wavenumber of the data depicted in (b), (d) visualizing the correlation factor (C_f) and determining the C_F -max through the newly established method.

Model parameters	True	Recovered	
		15% RGN	15% WGN
K (mV)	250	306.56	293.3108
z_0 (m)	4	4.8	5.1
x_0 (m)	-25	-25	-25
q	0.5	0.5	0.5
θ (°)	-75	-71.65	-71.13
C_F -max		0.5462	0.5876

Table 7. The authentic and retrieved model parameters pertaining to the second theoretical example (self-potential composite anomaly induced by vertical cylinder and first order regional source) contaminated with 15% RGN and 15% WGN.

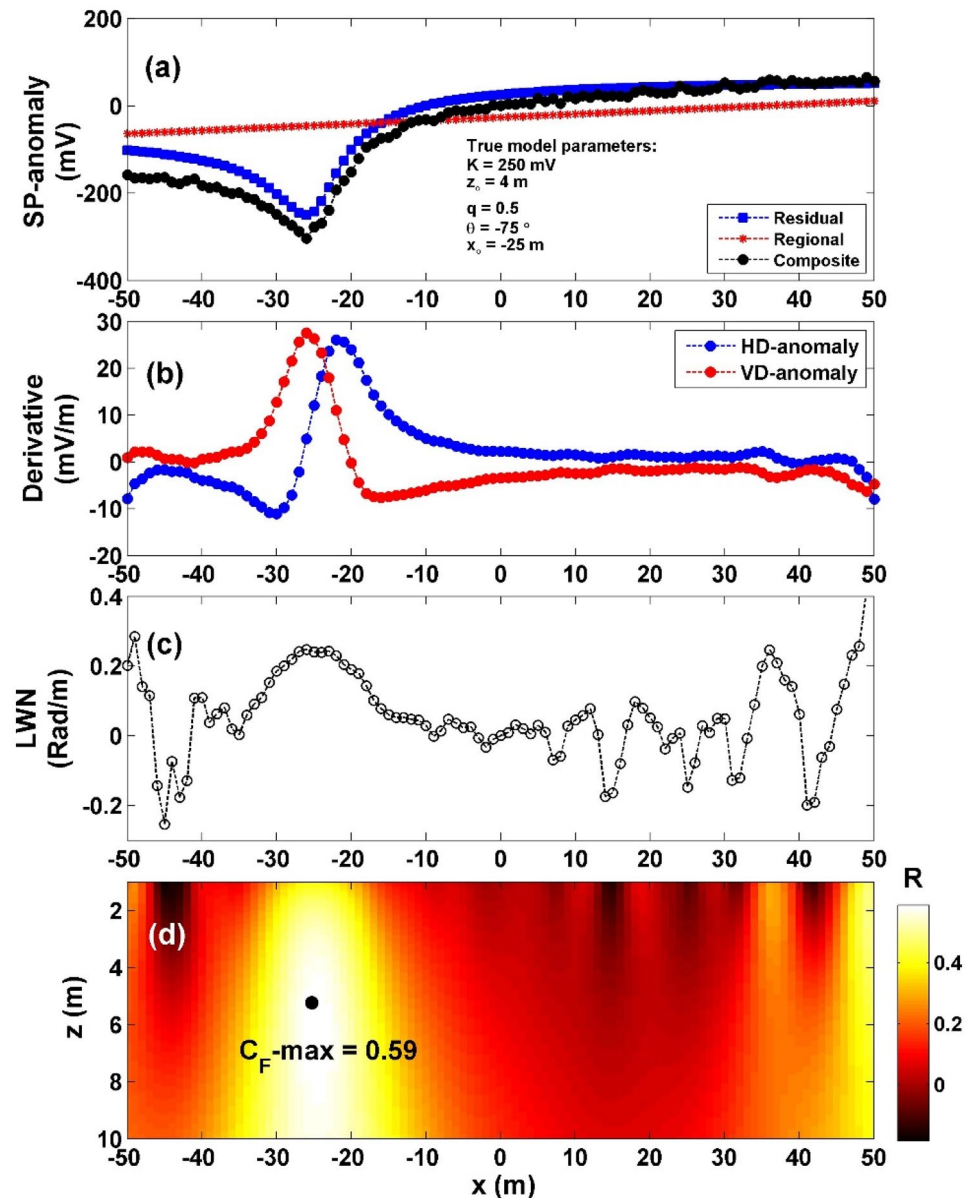


Figure 11. (a) Profile of the self-potential anomaly depicted in Fig. 9a after contaminating with 15% WGN, (b) computed horizontal and vertical derivatives for the profile depicted in (a), (c) local wavenumber of the data depicted in (b), (d) visualizing the correlation factor (C_F) and determining the C_F -max through the newly established method.

The heightened thermal maturity of organic materials in the Lias-epsilon black shales is commonly associated with the intrusion of the Bramsche Massif into the Earth's crust. Notably, strong gravity and magnetic anomalies, along with increased coal maturity in the Westphal D coals found in areas such as Ibbenbüren's mining region, are linked to the presence of the Bramsche Massif^{49–52}. The thermal heating of the stratigraphic series likely commenced before the Alp era and extends beyond Mesozoic black shales (2–5% C-org) of the Lower Toarcium and Lias-epsilon, as indicated by Mann⁵³. The contemporary morphology of the region has been significantly influenced by Pliocene tectonism and Quaternary sedimentation, as highlighted by studies such as those conducted by^{54,55}.

The survey area's location is depicted in Fig. 13^{45,49}. A self-potential profile was carried out across a 500 m span over the conductivity anomaly, specifically the Lias-epsilon black shales^{45,56} (Fig. 14a). The interpretation process began by calculating both the horizontal and vertical gradients of the observed anomaly, as illustrated in Fig. 14b. Subsequently, Eq. (4) was utilized to determine the value of LW_{mea} , as depicted in Fig. 14c. Advancing further, Eq. (7) was applied to calculate C_F , shown in Fig. 14d, with consideration for various q values outlined in Table 10. It is important to note that Table 10 highlights the maximum value of C_F (C_F -max = 0.71), denoted by a black circle in Fig. 14d. This corresponds to $K = 11,052.05 \text{ mV m}$, $z_o = 19 \text{ m}$, $x_o = 250 \text{ m}$, $q = 1$, and $\theta = -100^\circ$ (refer to Table 11). The comparison between the results obtained by our suggested approach and those obtained

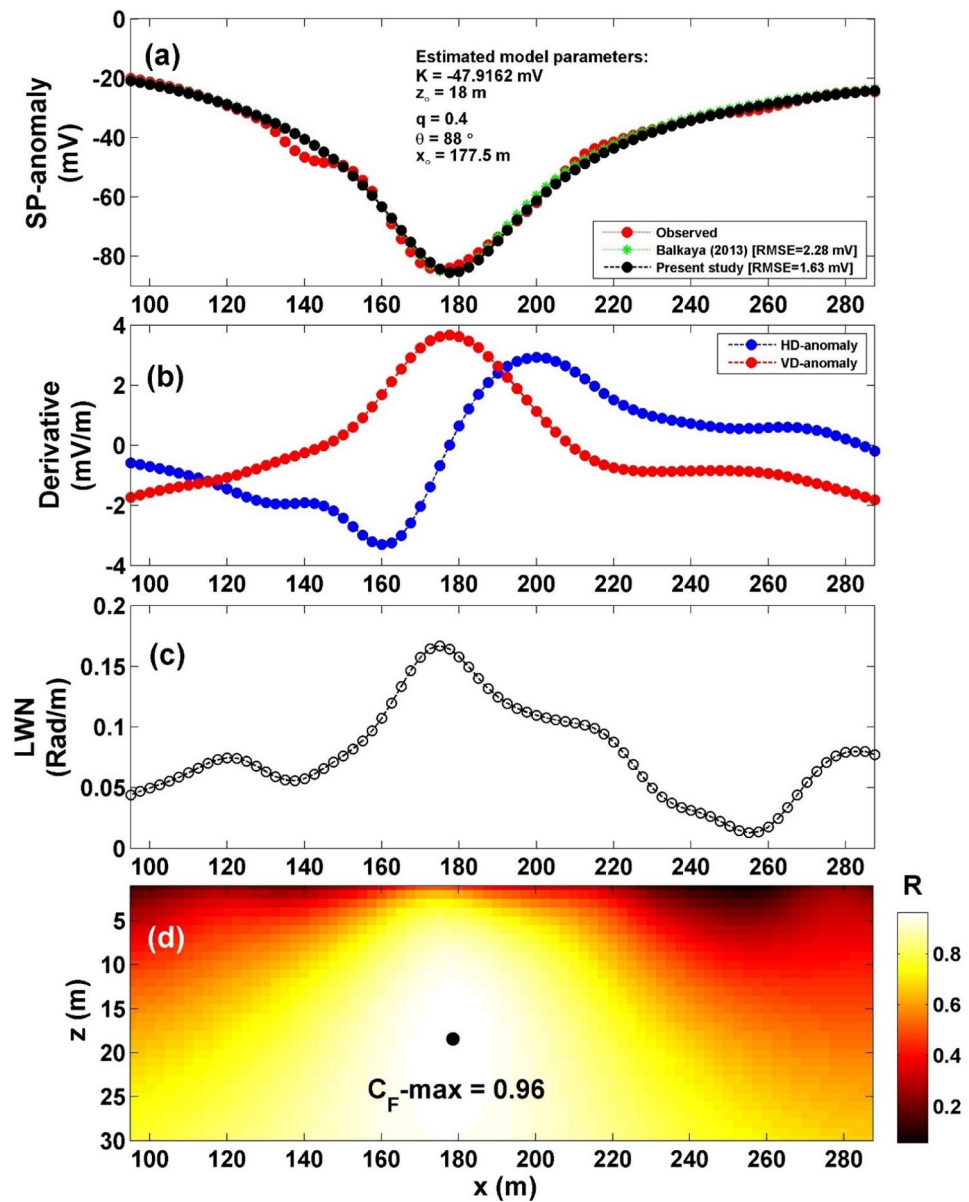


Figure 12. (a) Profile of the self-potential anomaly over Neem-Ka-Thana Copper Belt in India, along with the calculated responses from the present study and those obtained by Balkaya⁴⁴. (b) Computed horizontal and vertical derivatives for the profile depicted in (a), (c) local wavenumber of the data depicted in (b), (d) visualizing the correlation factor (C_F) and determining the C_F -max through the newly established method.

Geometric shape factor	Maximum correlation factor
(q)	(C_F -max)
0.5	0.9630
1	0.9628
1.5	0.9579

Table 8. The correlation factor (C_F) calculated at the different shape factors for the Neem-Ka-Thana Copper Belt field example in India. The optimum values are in [bold].

Model parameters	Balkaya ⁴⁴	Göktürkler and Balkaya ⁴¹			Biswas ⁴	Sungkono ⁴³		Present study
		GA	PSO	SA	(2017)	MDE	μJADE	
K (mV)	-48.50	-53.99	-49.53	-44.62	32.2	-48.38	-49.93	-47.92
z_o (m)	17.3	18.6	17.6	16.34	10.8	18.81	17.91	18.00
x_o (m)	176.8	176.84	176.77	176.92	177.8	178.32	176.66	177.5
q	0.4	0.42	0.4	0.38	0.5	0.41	0.41	0.40
θ (°)	88.05	87.83	88	88.25	89.6	88.95	88.06	88.00

Table 9. Retrieved model parameters for the Neem-Ka-Thana Copper Belt field example in India, and the comparison of the inverted results between the proposed method and those of different methods found in the literature.

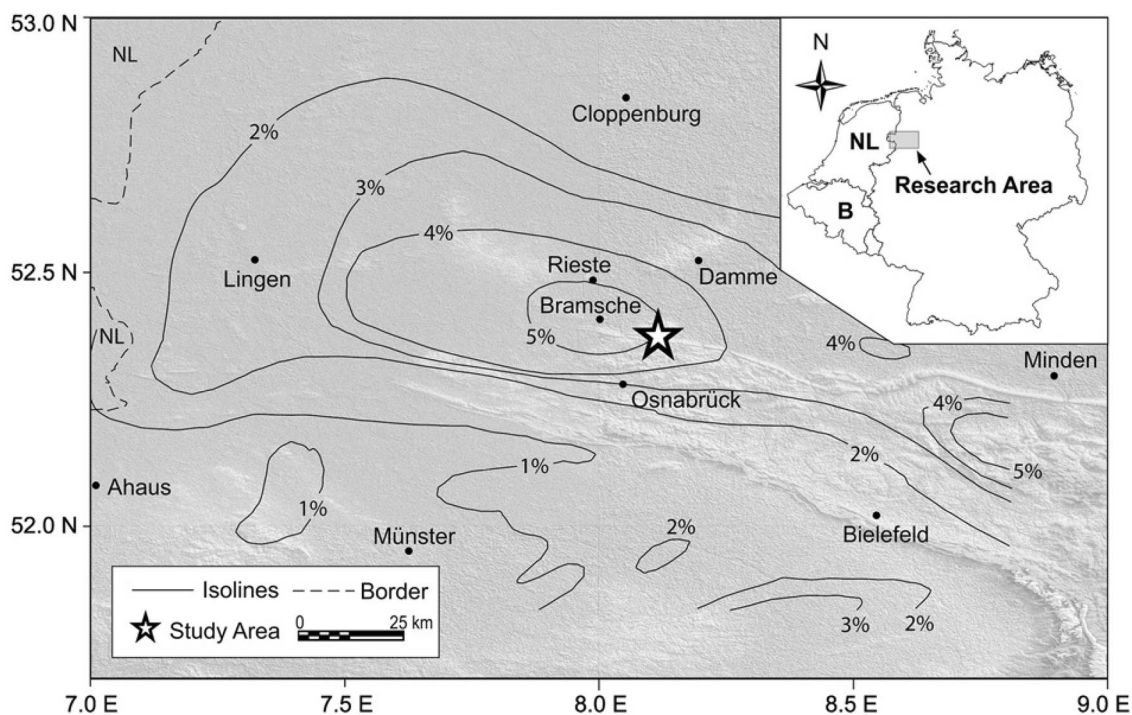


Figure 13. Location map of the of the survey area for the Osnabrück in Germany (after Stadler and Teichmüller⁴⁹ and Gurk et al.⁴⁵). NL Netherlands, B Belgium.

by Mehane et al.⁵⁷ is depicted in Fig. 14a. Table 11 provides a comparison of the inverted parameters between the proposed method and those from different methods documented in the literature. Also, Figs. 15 and 16 show the depth estimation from the 2D electrical resistivity tomography and the estimated source model using the suggested technique, respectively (taking into consideration the topography of the area). The results from the 2D electrical resistivity tomography and our method match well.

USA field example (Hi'iaka eruption)

On May 5, 1973, a dike penetrated the upper crust of Kilauea volcano within the geologic context of the east rift zone⁵⁸. This intrusion coincided with the eruption of Hi'iaka and Pauahi craters, as documented by Klein et al.⁵⁹ and Tilling et al.⁶⁰. The dike induced the formation of a surface fissure, stretching 100 m, which erupted magma west-southwest (WSW) of Hi'iaka crater. Geophysical measurements indicated that the dike extended underground in the WSW direction for an additional 1.5 km⁵⁸.

The SP profile's location is depicted in Fig. 17⁵⁸. The selected profile was carried out in 1997⁵⁸, spanning a length of 650 m (see Fig. 18a). The process of interpretation commenced by computing both the horizontal and vertical gradients of the observed anomaly, as depicted in Fig. 18b. Subsequently, Eq. (4) was applied to ascertain the value of LW_{mea} , as illustrated in Fig. 18c. Progressing further, Eq. (7) was employed to compute C_f as shown in Fig. 18d, considering various q values outlined in Table 12. It is noteworthy that Table 12 highlights the maximum value of C_f ($C_f\text{-max} = 0.89$), represented by a black circle in Fig. 17d. This corresponds to $K = -4688.45 \text{ mV m}^{2q-1}$, $z_o = 110 \text{ m}$, $x_o = 320 \text{ m}$, $q = 0.7$, and $\theta = -110^\circ$ (refer to Table 13). The comparison between the results obtained by our suggested method and those obtained by Mehane et al.⁵⁷ is depicted in

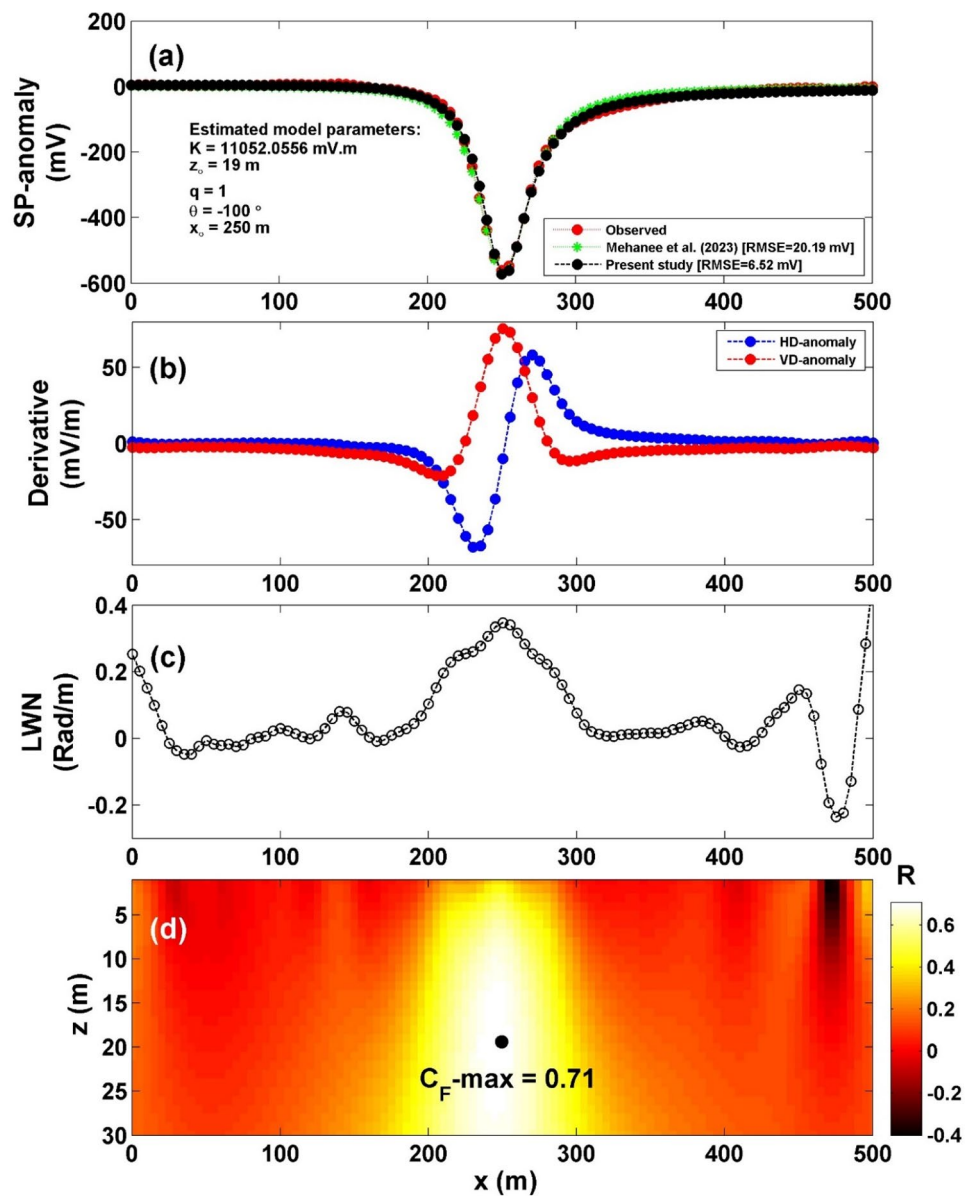


Figure 14. (a) Profile of the self-potential anomaly over Lias-epsilon black shales in Germany, along with the calculated responses from the present study and those obtained by Mehane et al.⁵⁷. (b) Computed horizontal and vertical derivatives for the profile depicted in (a), (c) local wavenumber of the data depicted in (b), (d) visualizing the correlation factor (C_f) and determining the C_F -max through the newly established method.

Geometric shape factor	Maximum correlation factor
(q)	(C_F -max)
0.5	0.6033
1	0.7089
1.5	0.7084

Table 10. The correlation factor (C_f) calculated at the different shape factors for the Lias-epsilon black shales field example in Germany. The Optimum values are in [bold].

Model parameters	Gurk et al. ⁴⁵	Mehanee ⁶¹	Mehanee et al. ⁵⁷	Present study
K (mV m^{2q-1})	- 48.50 (mV)	11,783.60 (mV m)	46,527 ($\text{mV m}^{1.4}$)	11,052.05 (mV m)
z_o (m)	10–23	19.9	23	19.00
x_o (m)	251.73	–	250	250.00
q	Thin sheet	1.0	1.2	1.0
θ ($^\circ$)	95	- 99.2	- 97	- 100.00

Table 11. Retrieved model parameters for Lias-epsilon black shales field example in Germany, and the comparison of the inverted results between the proposed method and those of different methods found in the literature.

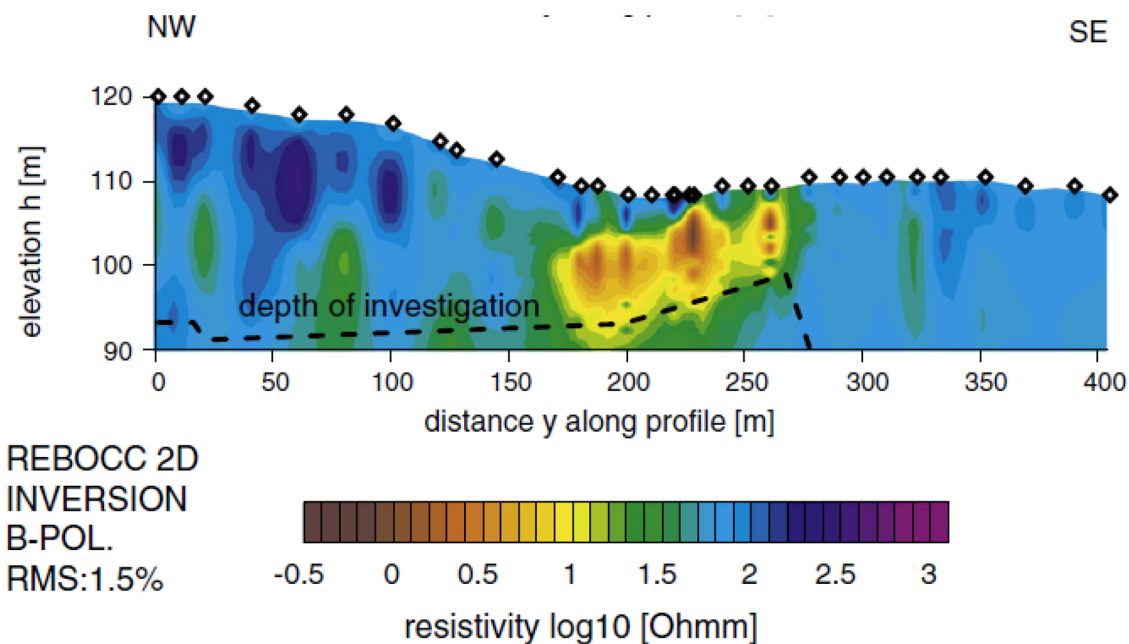


Figure 15. Results of the 2D electrical resistivity tomography inversion cross-section for the Osnabrück anomaly in Germany. (modified from Gurk et al.⁴⁵).

Fig. 18a. Table 13 presents a comparison of the inverted parameters between the proposed method and those documented in the literature from different methods.

Conclusions

In this study, we implemented an effective inversion imaging algorithm to characterize self-potential data originating from diverse sources such as spheres, vertical cylinders, and horizontal cylinders. The demonstrated algorithm holds promise for applications in mineral, ore exploration, and geothermal investigation offering precise predictions of various structural parameters—namely, amplitude factor (K), depth (z_o), body origin (x_o), shape factor (q), and polarization angle (θ)—with high accuracy and without the need for a priori information. The suggested algorithm employs the correlation factor (C_f) between the local wavenumber of the observed self-potential field and that of the computed field. The findings indicate that the maximum C_f (C_{F-max}) corresponds to the most reliable estimated model. Moreover, our proposed approach presents an imaging algorithm that provides rapid (within seconds) and robust imaging for subsurface depth and the location of concealed anomalous sources. To validate the efficiency, accuracy, and stability of the proposed algorithm, we subjected it to testing using three synthetic cases, including a pure data, a noisy data contaminated with different types of noise (RGN and WGN), an example for multi-source model and data with regional background effects. The applicability of the algorithm was further assessed through three real cases for mineral/ore exploration and geothermal investigation in India, Germany and USA. The resulting models from these real cases exhibited strong correlations with drilling data and findings reported in the literature. Finally, our study supports the suitability of the proposed algorithm for mineral/ore deposits exploration and geothermal investigation as well.

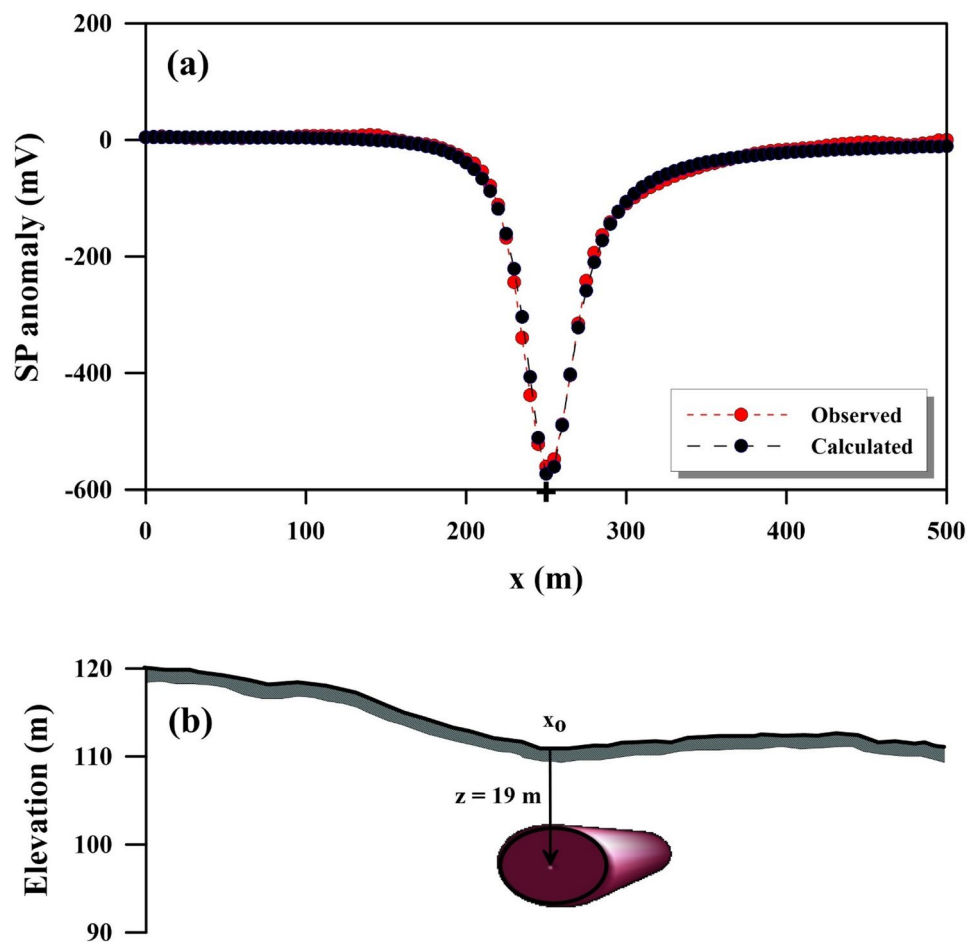


Figure 16. Estimated subsurface model using our suggested technique for the Osnabrück anomaly in Germany, taking into consideration the surface topography (b). The plus sign indicates the center location of source anomaly (a).

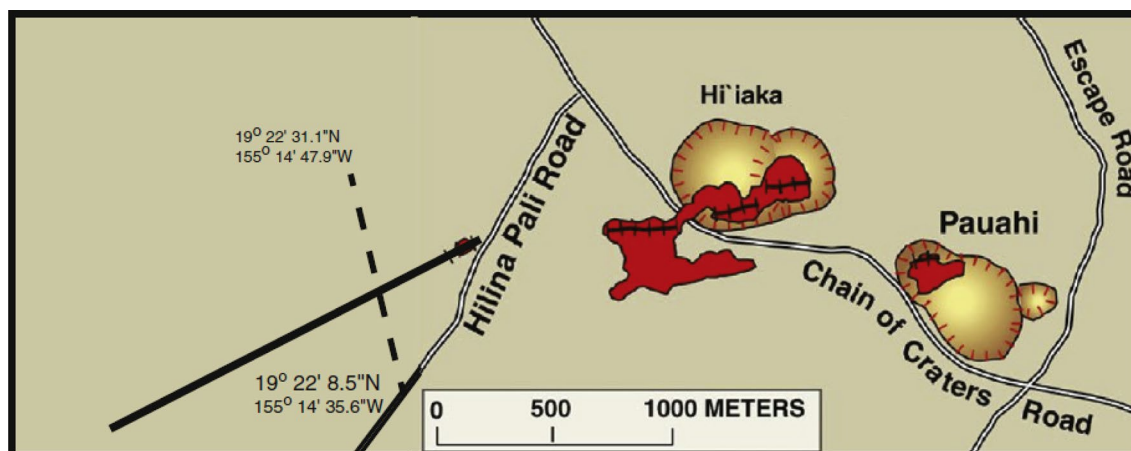


Figure 17. Location map of the of the SP profile for the Hi'iaka eruption in USA (after Davis⁵⁸).

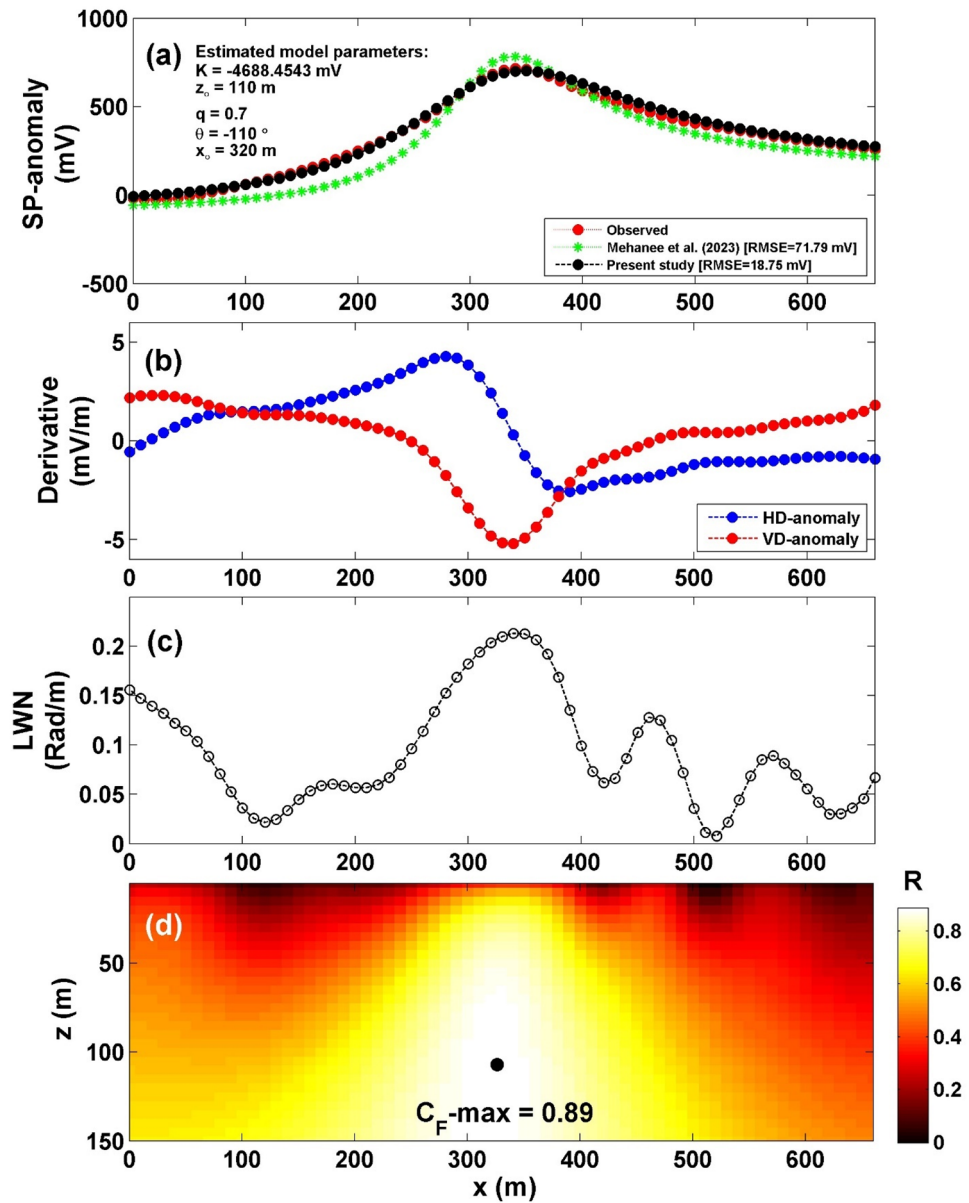


Figure 18. (a) Profile of the self-potential anomaly over Hi'iaka eruption in USA, along with the calculated responses from the present study and those obtained by Mehane et al.⁵⁷. (b) Computed horizontal and vertical derivatives for the profile depicted in (a), (c) local wavenumber of the data depicted in (b), (d) visualizing the correlation factor (C_F) and determining the $C_F\text{-max}$ through the newly established method.

Geometric shape factor	Maximum correlation factor
(q)	($C_F\text{-max}$)
0.5	0.8902
1	0.8876
1.5	0.8858

Table 12. The correlation factor (C_F) calculated at the different shape factors for the Hi'iaka eruption field example in USA. The Optimum values are in [bold].

Model parameters	Davis ⁵⁸	Mehanee et al. ⁵⁷	Present study
K (mV m ^{2q-1})	–	– 4340	– 4688.45
z ₀ (m)	120	69	110.00
x ₀ (m)	–	310	320.00
q	Dike model	0.7	0.70
θ (°)	–	– 110	– 110.00

Table 13. Retrieved model parameters for the Hi'iaka eruption field example in USA, and the comparison of the inverted results between the proposed method and those of different methods found in the literature.

Data availability

The datasets used and/or analyzed during the current study available from the corresponding author on reasonable request.

Received: 8 January 2024; Accepted: 15 February 2024

Published online: 14 March 2024

References

1. Fox, R. W. On the electromagnetic properties of metalliferous veins in the mines of Cornwall. *Philos. Trans. R. Soc.* **120**, 399–414 (1830).
2. Sill, W. R. Self-potential modeling from primary flows. *Geophysics* **48**, 76–86 (1983).
3. Revil, A., Finizola, A. & Gresse, M. Self-potential as a tool to assess groundwater flow in hydrothermal systems: A review. *J. Volcanol. Geothermal Res.* **437**, 107788 (2023).
4. Biswas, A. A review on modeling, inversion and interpretation of self-potential in mineral exploration and tracing paleo-shear zones. *Ore Geol. Rev.* **91**, 21–56 (2017).
5. Essa, K. S. Self potential data interpretation utilizing the particle swarm method for the finite 2D inclined dike: Mineralized zones delineation. *Acta Geodaetica Geophys.* <https://doi.org/10.1007/s40328-020-00289-2> (2020).
6. Elhussein, M. A novel approach to self-potential data interpretation in support of mineral resource development. *Nat. Resour. Res.* **30**, 97–127 (2021).
7. Yang, L. et al. Locating the source of self-potential using few-shot learning. *Eng. Appl. Artif. Intell.* **121**, 106045 (2023).
8. Corwin, R. F. & Hoover, D. B. The self-potential method in geothermal exploration. *Geophysics* **44**, 226–245 (1979).
9. Drahor, M. G. Application of the self-potential method to archaeological prospection: Some case histories. *Archaeol. Prospect.* **11**, 77–105 (2004).
10. Mehanee, S. Tracing of paleo-shear zones by self-potential data inversion: Case studies from the KTB, Rittsteig, and Grossensees graphite-bearing fault planes. *Earth Planets Sp.* **67**, 14–47 (2015).
11. Essa, K. S. & Elhussein, M. A new approach for the interpretation of self-potential data by 2-D inclined plate. *J. Appl. Geophys.* **136**, 455–461 (2017).
12. Tikhonov, A. N. & Arsenin, V. Y. *Solutions of Ill-Posed Problems* (Wiley, 1977).
13. Biswas, A. & Sharma, S. P. Resolution of multiple sheet-type structures in self-potential measurement. *J. Earth Syst. Sci.* **123**, 809–825 (2014).
14. Stoll, J., Bigalke, J. & Grabner, E. W. Electrochemical modelling of self-potential anomalies. *Surv. Geophys.* **16**, 107–120 (1995).
15. Essa, K. S. A new algorithm for gravity or self-potential data interpretation. *J. Geophys. Eng.* **8**, 434–446 (2011).
16. Sharma, S. P. & Biswas, A. Interpretation of self-potential anomaly over 2D inclined structure using very fast simulated annealing global optimization—an insight about ambiguity. *Geophysics* **78**, 3–15 (2013).
17. Kawada, Y. & Kasaya, T. Self-potential mapping using an autonomous underwater vehicle for the Sunrise deposit, Izu-Ogasawara arc, southern Japan. *Earth Planets Sp.* **70**, 142 (2018).
18. Lénat, J. F. Retrieving self-potential anomalies in a complex volcanic environment: An SP/elevation gradient approach. *Near Surf. Geophys.* **5**, 161–170 (2007).
19. Rittgers, J. B. et al. Self-potential signals generated by the corrosion of buried metallic objects with application to contaminant plumes. *Geophysics* **78**(5), 65–82 (2013).
20. Asfahani, J. & Tlas, M. Interpretation of self-potential anomalies by developing an approach based on linear optimization. *Geosci. Eng.* **5**, 7–21 (2016).
21. Paul, M. K. Direct interpretation of self-potential anomalies caused by inclined sheets of infinite extension. *Geophysics* **30**, 418–423 (1965).
22. Murthy, B. V. S. & Haricharan, P. Nomograms for the complete interpretation of spontaneous potential profiles over sheet like and cylindrical 2D structures. *Geophysics* **50**, 1127–1135 (1985).
23. Essa, K. S. Gravity data interpretation using the s-curves method. *J. Geophys. Eng.* **4**, 204–213 (2007).
24. Fedi, M. & Abbas, M. A. A fast interpretation of self-potential data using the depth from extreme points method. *Geophysics* **78**, E107–116 (2013).
25. El-Kaliouby, H. & Al-Garni, M. A. Inversion of self-potential anomalies caused by 2D inclined sheets using neural networks. *J. Geophys. Eng.* **6**, 29–34 (2009).
26. Minsley, B. J., Sogade, J. & Morgan, F. D. Three-dimensional self-potential inversion for subsurface DNAPL contaminant detection at the Savannah River Site, South Carolina. *Water Resour. Res.* **43**, W04429 (2007).
27. Patella, D. Introduction to ground surface self-potential tomography. *Geophys. Prospect.* **45**, 653–681 (1997).
28. Zhu, Z. et al. Self-potential tomography of a deep-sea polymetallic sulfide deposit on Southwest Indian Ridge. *J. Geophys. Res. Solid Earth* **125**, 14. <https://doi.org/10.1029/2020JB019738> (2020).
29. Jardani, A., Revil, A. & Dupont, J. P. Self-potential tomography applied to the determination of cavities. *Geophys. Res. Lett.* **33**, L13401. <https://doi.org/10.1029/2006GL026028> (2006).
30. Ma, G., Liu, C., Xu, J. & Meng, Q. Correlation imaging method based on local wavenumber for interpreting magnetic data. *J. Appl. Geophys.* **138**, 17–22 (2017).
31. Göktürkler, G. & Balkaya, C. Inversion of self-potential anomalies caused by simple-geometry bodies using global optimization algorithms. *J. Geophys. Eng.* **9**, 498–507 (2012).

32. Di Maio, R. *et al.* Quantitative interpretation of multiple self-potential anomaly sources by a global optimization approach. *J. Appl. Geophys.* **162**, 152–163 (2019).
33. Sungkono Warnana, D. D. Black hole algorithm for determining model parameter in self-potential data. *J. Appl. Geophys.* **148**, 189–200 (2018).
34. Santos, F. A. Inversion of self-potential of idealized bodies' anomalies using particle swarm optimization. *Comput. Geosci.* **36**, 1185–1190 (2010).
35. Agarwal, A., Chandra, A., Shalivahan, S. & Singh, R. K. Grey wolf optimizer: A new strategy to invert geophysical data sets. *Geophys. Prospect.* **66**, 1215–1226 (2018).
36. Biswas, A. A comparative performance of least square method and very fast simulated annealing global optimization method for interpretation of self-potential anomaly over 2-D inclined sheet type structure. *J. Geol. Soc. India* **88**, 493–502 (2016).
37. Essa, K. S., Diab, Z. E. & Mehane, S. A. Self-potential data inversion utilizing the Bat optimizing algorithm (BOA) with various application cases. *Acta Geophys.* **71**, 567–586 (2023).
38. Zhang, D., You, X., Liu, S. & Pan, H. Dynamic multi-role adaptive collaborative ant colony optimization for robot path planning. *IEEE Access* **15**(8), 129958e74. <https://doi.org/10.1109/ACCESS.2020.3009399> (2020).
39. Yüngül, S. Interpretation of spontaneous polarization anomalies caused by spherical ore bodies. *Geophysics* **15**, 237–246 (1950).
40. Elhussein, M. & Diab, Z. E. Gravity data imaging using local wavenumber-based algorithm: Sustainable development cases studies. *Nat. Resour. Res.* **32**, 171–193 (2023).
41. Nabighian, M. N. The analytic signal of two-dimensional magnetic bodies with polygonal cross-section: Its properties and use for automated anomaly interpretation. *Geophysics* **37**, 507–517 (1972).
42. Reddi, A. G. B., Madhusudan, I. C., Sarkar, B. & Sharma, J. K. *An Album of Geophysical Responses from Base Metal Belts of Rajasthan and Gujarat* (Geological Survey of India, 1982).
43. Sungkono, Robust interpretation of single and multiple self-potential anomalies via Cower pollination algorithm. *Arab. J. Geosci.* **13**, 1–16 (2020).
44. Balkaya, Ç. An implementation of differential evolution algorithm for inversion of geoelectrical data. *J. Appl. Geophys.* **98**, 160–175 (2013).
45. Gurk, M., Bosch, F. P. & Tougiannidis, N. Electric field variations measured continuously in free air over a conductive thin zone in the tilted Lias-epsilon black shales near Osnabrück, Northwest Germany. *J. Appl. Geophys.* **91**, 21–30 (2013).
46. Muñoz, Y. A., Littke, R., & Brix, M. R. Evolution of the Lower Saxony Basin and the Bramsche Massif. DFG-SPP 1135 “Dynamics of the Central European Basin System”. In *4th Rundgespräch Eringerfeld, Terra Nostra, Schriften der Alfred-Wegener-Stiftung*, 1–4 (2005).
47. Muñoz, Y. A.. The thermal history of the western Lower Saxony Basin. Germany, PhD Thesis RWTH Aachen, ISBN: 3-86130-884-3, 153 (2007).
48. Bilgili, F., Götze, H. J., Pasteka, R., Schmidt, S. & Hackney, R. Intrusion versus inversion—a 3D density model of the southern rim of the Northwest German Basin. *Int. J. Earth Sci.* **98**, 571–583 (2009).
49. Stadler, G., & Teichmüller, M. Zusammenfassender Überblick über die Entwicklung des Bramscher Massivs und des Niedersächsischen Tektogens. Fortschritte in der Geologie von Rheinland und Westfalen, 18. Geologischer Dienst Nordrhein-Westfalen-Landesbetrieb, Krefeld, 547–564 (1971a).
50. Stadler, G., & Teichmüller, M. Die Umwandlung der Kohlen und die Diagenese der Ton- und Sandsteine in der Untertagebohrung 150 der Steinkohlebergwerke Ibbenbüren. Fortschritte in der Geologie von Rheinland und Westfalen, 18. Geologischer Dienst Nordrhein-Westfalen-Landesbetrieb, Krefeld, 125–146 (1971b).
51. Teichmüller, R. & Teichmüller, M. Inkohlungsgradienten in der Anthrazitfolge des Ibbenbürener Karbons. *Fortsch. Geol. Rheinland Westfalen* **33**, 231–253 (1985).
52. Brink, H. J., Dürschner, H. & Trappe, H. Some aspects of the late and post-Variscan development of the Northwestern German Basin. *Tectonophysics* **207**, 65–95 (1992).
53. Mann, U. Veränderung von Mineralmatrix und Porosität eines Erdölmuttergesteins durch einen Intrusivkörper (Lias epsilon 2–3: Hilsmulde, NW-Deutschland). *Facies* **17**(1), 181–188 (1987).
54. Ehlers, J., Eissmann, L., Lippstreu, L., Stephan, H. J. & Wansa, S. Pleistocene glaciations of North Germany. In *Quaternary Glaciations—Extent and Chronology—A Closer Look* (eds Ehlers, J. *et al.*) 135–146 (Elsevier, 2011).
55. Skupin, K., Speetzen, E., & Zandstra, J. G. Die Eiszeit in Nordwestdeutschland—Zur Vereisungsgeschichte der Westfälischen Bucht und angrenzender Gebiete, Geologischer Dienst Nordrhein-Westfalen-Landesbetrieb, Krefeld, 49 Abb., 24 Tab., 2 Taf., 2 Ktn, 143 (1993).
56. Gurk, M. Eigenpotentialsonde zur schnellen Messung der elektrischen Potentialverteilung und Langzeitmessung des erdelektrischen Feldes. Gebrauchsmuster (Patent) Nr. 20 2007 003 079.1. Deutsches Patent und Markenamt, München, Germany (2007).
57. Mehane, S. A., Essa, K. S., Soliman, K. S. & Diab, Z. E. A fast imaging method for the interpretation of self-potential data with application to geothermal systems and mineral investigation. *Sci. Rep.* **13**, 13548. <https://doi.org/10.1038/s41598-023-39672-8> (2023).
58. Davis, P. M. Geothermal evolution of an intruded dike in the rift zone of Kilauea volcano, Hawaii from VLF and self-potential measurements. *J. Volcanol. Geotherm. Res.* **302**, 64–80 (2015).
59. Klein, F. W., Koyanagi, R. Y., Nakata, J. S., & Tanigawa, W. R. The seismicity of Kilauea's magma system. In *Volcanism in Hawaii: U.S. Geological Survey Professional Paper* (Decker, R. W., Wright, T. L., & Stauffer, P. H., eds.), Vol 1350, 1019–1185 (1987).
60. Tilling, R. I., Christiansen, R. L., Duffield, W. A., Endo, E. T., Holcomb, R. T., Koyanagi, R. Y., Peterson, D. W., & Unger, J. D. The 1972–1974 Mauna Ulu eruption, Kilauea Volcano: An example of quasi-steady-state magma transfer. In *Volcanism in Hawaii: U.S. Geological Survey Professional Paper* (Decker, R. W., Wright, T. L., & Stauffer, P. H., eds.), Vol. 1350, 405–469 (1987).
61. Mehane, S. A. Simultaneous joint inversion of gravity and self-potential data measured along profile: Theory, numerical examples, and a case study from mineral exploration with cross validation from electromagnetic data. *IEEE Trans. Geosci. Remote Sens.* **60**, 1–20 (2022).

Acknowledgements

The authors express their gratitude to the editor-in-chief, in-house editor and the two proficient reviewers for their enthusiastic engagement, valuable feedback on the manuscript, and contributions to enhancing this work.

Author contributions

M.E.: wrote the original manuscript draft, conceptualization, code, methodology, test the code validation, made the figures, tables, practical work and revised the manuscript. Z.E.D.: wrote the original manuscript draft, conceptualization, code, methodology, test the code validation, made the figures, tables, practical work and revised the manuscript.

Funding

Open access funding provided by The Science, Technology & Innovation Funding Authority (STDF) in cooperation with The Egyptian Knowledge Bank (EKB).

Competing interests

The authors declare no competing interests.

Additional information

Correspondence and requests for materials should be addressed to M.E. or Z.E.D.

Reprints and permissions information is available at www.nature.com/reprints.

Publisher's note Springer Nature remains neutral with regard to jurisdictional claims in published maps and institutional affiliations.



Open Access This article is licensed under a Creative Commons Attribution 4.0 International License, which permits use, sharing, adaptation, distribution and reproduction in any medium or format, as long as you give appropriate credit to the original author(s) and the source, provide a link to the Creative Commons licence, and indicate if changes were made. The images or other third party material in this article are included in the article's Creative Commons licence, unless indicated otherwise in a credit line to the material. If material is not included in the article's Creative Commons licence and your intended use is not permitted by statutory regulation or exceeds the permitted use, you will need to obtain permission directly from the copyright holder. To view a copy of this licence, visit <http://creativecommons.org/licenses/by/4.0/>.

© The Author(s) 2024